*J. Fluid Mech.* (2007), *vol.* 579, *pp.* 315–346.  
doi:10.1017/S0022112007005204 Printed in the United Kingdom

# Feedback control of subsonic cavity flows using reduced-order models

M. SAMIMY[1]†, M. DEBIASI[1]‡, E. CARABALLO[1], A. SERRANI[2], X. YUAN[2], J. LITTLE[1] AND J. H. MYATT[3]

[1]Gas Dynamics and Turbulence Laboratory; Department of Mechanical Engineering, Collaborative Center for Control Science, The Ohio State University, Columbus, Ohio 43235 USA, USA

[2]Department of Electrical and Computer Engineering, Collaborative Center for Control Science, The Ohio State University, Columbus, Ohio 43235 USA, USA

[3]Air Force Research Laboratory – Air Vehicles Directorate, Wright–Patterson AFB, USA

(Received 28 March 2006 and in revised form 23 November 2006)

Development, experimental implementation, and the results of reduced-order model based feedback control of subsonic shallow cavity flows are presented and discussed. Particle image velocimetry (PIV) data and the proper orthogonal decomposition (POD) technique are used to extract the most energetic flow features or POD eigenmodes. The Galerkin projection of the Navier–Stokes equations onto these modes is used to derive a set of nonlinear ordinary differential equations, which govern the time evolution of the eigenmodes, for the controller design. Stochastic estimation is used to correlate surface pressure data with flow-field data and dynamic surface pressure measurements are used to estimate the state of the flow. Five sets of PIV snapshots of a Mach 0.3 cavity flow with a Reynolds number of $10^5$ based on the cavity depth are used to derive five different reduced-order models for the controller design. One model uses only the snapshots from the baseline (unforced) flow while the other four models each use snapshots from the baseline flow combined with snapshots from an open-loop sinusoidal forcing case. Linear-quadratic optimal controllers based on these models are designed to reduce cavity flow resonance and are evaluated experimentally. The results obtained with feedback control show a significant attenuation of the resonant tone and a redistribution of the energy into other modes with smaller energy levels in both the flow and surface pressure spectra. This constitutes a significant improvement in comparison with the results obtained using open-loop forcing. These results affirm that reduced-order model based feedback control represents a formidable alternative to open-loop strategies in cavity flow control problems even in its current state of infancy.

## 1. Introduction

The goals of the flow control are extensive as exhibited by its multitude of applications (e.g. lift increase, drag reduction, mixing enhancement, laminar-to-turbulent transition delay, separation control, noise suppression). Flow control can be divided into two general categories of passive or active control. In passive control, which is straightforward to implement and has widespread applications, control is

† Author to whom correspondence should be addressed: Samimy.1@osu.edu.
‡ Present address: Temasek Laboratories, National University of Singapore.

accomplished by geometrical modifications to the flow system. In active control, external energy (mass and/or momentum, heat) is added to the flow. Active control is divided into open-loop and closed-loop. In open-loop control, actuation takes place based on an operator's command or a predetermined input. In the closed-loop or feedback control case, which is the subject of the current work, information from one or more sensors in the flow along with a flow model guides the actuation process. Based on the frequency content of actuation relative to instability frequencies of the flow, active control can be further divided into two categories. The first category involves steady or low-frequency (frequencies much lower than any flow instability frequencies) energy addition. The second category employs actuators with large bandwidths that include at least one flow instability frequency.

Successful applications of feedback control are widespread in areas such as robotics, aerospace, telecommunication, transportation systems manufacturing systems and chemical processes. Only in recent years has feedback control of aerodynamic flows received focused attention (Cattafesta *et al.* 1997, 2003; Gad-el-Hak 2000; Williams, Fabris & Morrow 2000; Kegerise, Cattafesta & Ha 2002; Rowley & Williams 2003; Samimy *et al.* 2003; Siegel *et al.* 2003; Gerhard *et al.* 2003; Glauser *et al.* 2004; Tadmor *et al.* 2004). Open-loop flow control, which can be useful in many applications, lacks the responsiveness and flexibility needed for application in dynamic flight environments. In contrast, closed-loop flow control is well-suited to the successful management of these flows since it allows adaptability to variable conditions. In addition, closed-loop control shows the potential to significantly reduce power requirements in comparison to open-loop control strategies (Cattafesta *et al.* 1997). Unfortunately, the tools of classical control system theory are not directly applicable to aerodynamic flows since such systems display spatial continuity and nonlinear behaviour while also posing formidable modelling challenges owing to their infinite dimensionality, a complexity introduced by the Navier–Stokes equations. In order to design and successfully implement a closed-loop control strategy, it is necessary to obtain a reduced-order dynamical model of the flow, which can capture the important dynamics of the flow and actuation while remaining sufficiently simple to allow its use in model-based feedback control design.

The flow over a shallow cavity – a configuration relevant to many practical applications that has been extensively studied – was selected for the present study. This flow is characterized by a strong coupling between the flow dynamics and the flow-generated acoustic field that can produce self-sustained resonance known to cause, among other problems, store damage and airframe structural fatigue in weapons bays. A comprehensive review of this phenomenon and of various control and actuation strategies developed for its suppression is given in Cattafesta *et al.* (2003) and Rowley & Williams (2006).

Rossiter (1964) first developed an empirical formula, which was later modified and improved by Heller & Bliss (1975), for predicting the frequencies of cavity flow resonance, today referred to as Rossiter frequencies or modes. Rossiter also investigated the concept of a dominant mode of oscillation that was later observed by others to coincide with the natural longitudinal cavity acoustic mode (Rockwell & Naudascher 1978). In such a condition, a strong single-mode resonance occurs (Williams *et al.* 2000); otherwise multiple modes exist in the flow. A similar interaction can also occur between Rossiter modes and the natural transversal cavity acoustic modes (e.g. Ziada, Ng & Blake 2003; Debiasi & Samimy 2004). Recent theoretical models of cavity acoustic resonance based on edge scattering processes explain these behaviours (Kerschen & Tumin 2003; Alvarez, Kerschen & Tumin 2004; Alvarez &

Kerschen 2005). Rapid switching between modes has been observed in multi-mode conditions (Cattafesta *et al.* 1998; Williams *et al.* 2000; Debiasi *et al.* 2004). The rapid and seemingly random switching between multiple modes places large bandwidth and fast time response requirements on both the actuation scheme and feedback control algorithm.

Extensive work has been carried out to control the flow over a cavity. Passive techniques include rigid fixed fences, spoilers, ramps (Heller & Bliss 1975; Sarno & Franke 1994; Ukeiley *et al.* 2002) and cylinders or rods placed in the boundary layer near the leading edge of the cavity (McGrath & Shaw 1996; Stanek *et al.* 2003). These devices are simple, inexpensive and reliable, but may not work well at off-design conditions since they have little or no capability for adjustment to changing flow conditions. Different open-loop control strategies have been used with varying degrees of success (e.g. Shaw 1998; Stanek *et al.* 2003; Grove, Leugers & Akroyd 2003; Debiasi & Samimy 2004). There have also been significant efforts to investigate closed-loop control approaches (Cattafesta *et al.* 1997, 1999; Shaw & Northcraft 1999; Williams *et al.* 2000, 2002; Kegerise *et al.* 2002; Rowley *et al.* 2002; Cabell *et al.* 2002; Caraballo *et al.* 2005, 2006). The results of these closed-loop endeavours are encouraging, but also indicate that many issues remain to be resolved and numerous opportunities exist for further advancement of the technology.

Although we have examined other control approaches in recent years (Debiasi *et al.* 2004; Efe *et al.* 2005; Yan *et al.* 2006), our primary objective from the onset has been the development of control techniques based on reduced-order models of the cavity flow (Samimy *et al.* 2004; Yuan *et al.* 2005; Caraballo *et al.* 2005, 2006). The approach we have followed in the development of such a model is based on the proper orthogonal decomposition (POD) method. This technique relies on the energy-containing eddies in the flow that can be extracted using the spatial correlation tensor of the velocity field in the form of spatial eigenmodes called POD modes. These structures are the most dominant features in the flow and arguably are the only entities that can effectively be controlled. The dynamics of the flow are obtained when these modes are modulated by modal coefficients obtained by projecting the governing Navier–Stokes equations onto the POD basis. This results in a set of nonlinear ordinary differential equations, which we use for controller design. The equations are autonomous and not useful for controller design purposes since the controller input is not explicit. Consequently, they must be recast in a form expressing the control input explicitly so that a feedback controller can be designed using the tools of control theory (Efe & Özbay 2003; Caraballo *et al.* 2005).

In § 2, we introduce the flow facility used in this work. In § 3, we present the POD and Galerkin methods adopted for deriving the reduced-order model, and the stochastic estimation approach used for real-time estimation of the flow model variables directly from dynamic surface pressure measurements. This is followed in § 4 by a discussion of the flow characteristics and of the reduced-order model results and in § 5 by the design and implementation of the linear-quadratic controller. We will present and discuss the experimental results in § 6, followed by concluding remarks in § 7.

## 2. Experimental facility and techniques

The experimental facility is a small-scale blow-down wind tunnel located at the Gas Dynamics and Turbulence Laboratory of The Ohio State University. The tunnel can be operated continuously using filtered and dried air, which is supplied by

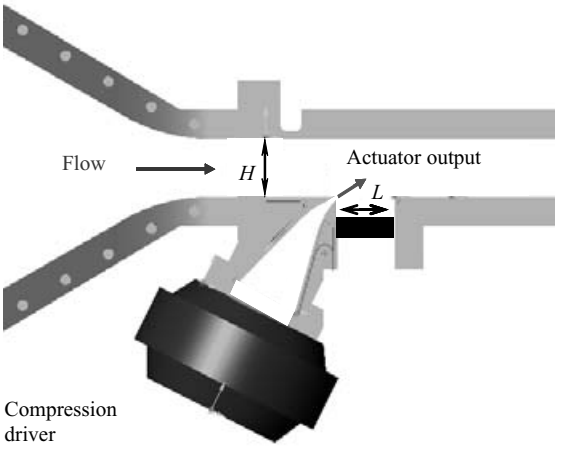


FIGURE 1. Scaled drawing of the experimental set-up showing the test section with the cavity and the actuator.

two four-stage compressors and stored in two large tanks of 1600 $m^3$ volume at approximately 16 MPa. The air is conditioned in the settling chamber and passed through various screens designed to minimize free-stream turbulence. Flow is directed to the 50.8 mm (2 in) by 50.8 mm (2 in) test section (figure 1) through a smoothly contoured converging nozzle and exhausts to the atmosphere through a large pipe. The facility operates in the Mach number range 0.2 to about 0.7. A 50.8 mm (2 in) long variable depth cavity is recessed in the floor of the wind tunnel. This cavity spans the entire width of the test section. The focus of this work is on a shallow cavity with a depth of 12.7 mm (0.5 in) corresponding to a cavity aspect ratio, $L/D$, of 4. For Mach 0.3 flow, the Reynolds number based on this cavity depth is about $10^5$. Optical quality windows surround the test section and allow laser-based flow diagnostics from 15 mm upstream to 25 mm downstream of the cavity. Additional details of the facility and the experimental techniques used can be found in Debiasi & Samimy (2004) and Little, Debiasi & Samimy (2006).

The control flow is produced by mechanical oscillation of the titanium diaphragm of a Selenium D3300Ti compression driver. The flow is channelled to the cavity leading edge where it exits at an angle of 30° with respect to the main flow through a two-dimensional slot of 1 mm height spanning the cavity width (figure 1). This arrangement provides zero net mass, non-zero net momentum flow for actuation, similar to that of a synthetic jet. Effective actuation can be achieved in the frequency range of 1–5 kHz, which is a clear advantage of this actuator over a traditional synthetic jet. Primarily owing to the geometry of the actuator plenum, the jet velocity output has significant frequency modulation with several peaks and valleys in the range of 1–10 kHz. Conversely, at all frequencies the amplitude response is approximately a linear function of the input voltage level (Debiasi & Samimy 2004). Based on our previous observations, the modulated frequency response of the actuator has a minor impact on the results with sinusoidal forcing since the actuator exhibits good authority and produces conspicuous effects even at frequencies where its maximum output velocity is quite small (5 m $s^{-1}$ in comparison with a peak of about 25 m $s^{-1}$). However, the actuator transfer function can produce a selective amplification at some output frequencies when broadband control signals are supplied. This undesirable characteristic is being addressed by a compensator currently under development (Kim

*et al.* 2007). In the current work, the actuator input voltage is produced by either a BK Precision 3011A function generator for open-loop forcing or by a dSPACE 1103 digital signal processor (DSP) control board in closed-loop studies and is amplified by a Crown D-150A amplifier in either case. The momentum coefficient of the actuator, $C_\mu = hu_{rms}^2/HU_\infty^2$, is in the range of $10^{-4}$ to $10^{-6}$, where $u_{rms}$ is the root-mean-square forcing flow velocity at the actuator exit slot, $U_\infty$ is the velocity of the free stream in the test section above the cavity, and $h$ and $H$ are the actuator exit slot and wind-tunnel test-section height, respectively.

The instantaneous features of the flow in a streamwise plane at the test-section centreline are visualized using laser-sheet diagnostics. Scattering of incident radiation is accomplished by locally seeded smoke particles introduced through a narrow (3 mm) streamwise slot on the cavity floor. The laser sheet enters the test section from an optical window on the top wall of the tunnel and exits through the slot on the cavity floor. The laser is a Continuum Powerlite 8010 Nd:YAG pulsed laser operating at the second harmonic (532 nm) with 9 ns pulse duration at 10 Hz. A Princeton Instruments intensified CCD camera is used to obtain flow images. The laser and camera are phase-locked to the resonant or actuation frequency using a reference signal provided by a timing card (National Instruments PC-T10-10) to obtain phase-averaged data.

Planar snapshots of the velocity field, required for the development of the reduced-order model, are acquired using a two-component LaVision particle image velocimetry (PIV) system. The flow is uniformly seeded upstream of the stagnation chamber with di-ethyl-hexyl-sebacat particles using a four-jet atomizer. A dual-head Spectra Physics PIV-400 Nd:YAG laser operating at the second harmonic (532 nm) at approximately 100 mJ per pulse is used in conjunction with sheet-forming optics to form a thin ($\sim$1 mm) sheet on the $(x, y)$-plane passing through the centreline of the cavity. The narrow slot cut into the cavity floor minimizes beam reflections by allowing the laser sheet to exhaust and diffuse in a sealed light trap. Two images separated by 1.8 µs corresponding to the pulses from each laser head are acquired by a $2000 \times 2000$ pixel Redlake CCD camera with a 90 mm macro lens and a narrow band-pass optical filter. The camera views the streamwise laser sheet orthogonally over the entire test-section length as in the flow-visualization case. A computer with dual Intel Xeon processors is used for data acquisition. The acquired images are divided into $32 \times 32$ pixel interrogation windows which contain of the order of 6–10 particles each. For each image, subregions are cross-correlated using multi-pass processing with 50 % overlap. The resulting vector fields are post-processed to remove any remaining spurious vectors. This arrangement gives a velocity vector grid of $128 \times 128$ over the approximate measurement domain of 50.8 mm (2 in) $\times$ 50.8 mm (2 in), which translates to velocity vectors separated by about 0.4 mm. A comparison between ensemble average streamwise velocity profiles measured with the PIV system and Pitot probe for Mach 0.3 flow (not shown) confirms that the two measurements agree within 1 % in the free stream. Phase-locked PIV is accomplished by synchronizing the image-acquisition process to a timing card signal as in the flow-visualization case.

Flush-mounted Kulite transducers are placed at various locations on the surfaces of the test section for dynamic pressure measurements. Figure 2 shows the locations of the six transducers on the cavity sidewall used in this study. Transducers 7–9 in the cavity floor are shown as well, which were also used for measurements not requiring the use of the slotted cavity floor. The transducers have a flat frequency response up to about 50 kHz, and are powered by a signal conditioner that amplifies and low-pass filters the signals below 10 kHz. Additional high-pass filtering removes low-frequency noise below 100 Hz. For spectral analysis, 262 144 samples are acquired at 200 kHz


FIGURE 2. Position of the Kulite pressure transducers 1–6 (on the sidewall) and of transducers 7–9 in the cavity floor.

rate through a 16-bit acquisition board (National Instruments PCI-6143 S-Series) operating on a Dell Precision Workstation 650 computer. By using the transducer sensitivity and accounting for the amplifier gain setting, the voltage values of the time traces are converted to non-dimensional pressure referenced to the commonly used value of 20 μPa. Short-time Fourier transform (STFT) is used to obtain information on the time evolution of the sound pressure levels (SPL) (Hammond & White 1996; Qian & Chen 1996; Little *et al.* 2006), and SPL spectra are obtained by averaging the corresponding spectrograms.

For state estimation, dynamic pressure measurements are acquired simultaneously with the PIV measurements. In the current study, 1000 PIV snapshots were recorded for each flow/actuation condition explored. The PIV snapshots are time-uncorrelated since they are sampled at a rate of 5 Hz which is dictated by the 10 Hz laser, CCD camera, and data acquisition system. For each PIV snapshot, 128 samples from each of the transducers 1–6 in figure 2 are acquired at 50 kHz rate. A programmable timing unit (PTU) housed in the PIV computer, triggers the acquisition of pressure data corresponding to each PIV snapshot. The temporal location of the laser pulse with respect to the pressure traces is resolved by acquiring the laser Q-switch TTL simultaneously with the pressure signals. The experiment is designed in such a way that the Q-switch TTL falls near the middle of a pressure data sequence. This simultaneous sampling of the laser Q-switch signal and the pressure signals allows, for each snapshot, the identification of the section of pressure time traces corresponding to the instantaneous velocity field. The Q-switch TTL corresponding to only one laser pulse is sufficient due to the small accurate time separation between laser pulses.

To quantitatively characterize the frequency content of cavity shear layer for baseline and controlled cases, hot-wire measurements are employed at three streamwise locations, $x/D = 1$, 2 and 3. Velocity time traces are acquired using a TSI 1276-10A subminiature hot-film probe connected to a TSI 1750 constant-temperature anemometer. The 25 μm thick and 0.25 mm long sensor has a flat frequency response up to about 40 kHz and can accurately resolve frequencies up to 10 kHz. Similar to the pressure case, 262 144 samples of the signal from the anemometer are acquired at 200 kHz. For each streamwise location, the optimal vertical position for clearest description of the structure frequency content was determined by analysing vertically

traversed velocity spectra. For the Mach 0.3 flow, the optimal vertical positions are respectively 4, 6 and 8 mm above the cavity leading edge, a result consistent with observations of Hussain & Zaman (1985) for a plane mixing layer.

For closed-loop control of the flow, the dSPACE 1103 DSP board is used. This system uses four independent, 16-bit A/D converters each with 4 multiplexed input channels that allow simultaneous acquisition and control processing of 4 signals. It also allows, almost simultaneous, because of multiplexing, acquisition and processing of additional signals at a rate up to 50 kHz per channel to produce at the same rate a control signal from a 14-bit output channel. As before, the pressure signals are band-pass filtered between 100 Hz and 10 kHz to remove unwanted frequency components.

## 3. Reduced-order modelling procedure

Development of tools and procedures for feedback control based on reduced-order models has been our primary goal from the onset of this research programme (Caraballo *et al.* 2004; Samimy *et al.* 2004; Yuan *et al.* 2005). Our recent work has focused on deriving the reduced-order models of the cavity flow from PIV and surface pressure measurements (Caraballo *et al.* 2005, 2006). The overall technique combines three separate methods and procedures to obtain a reduced-order model for the design and implementation of a controller. First, the proper orthogonal decomposition method is used to obtain spatial eigenmodes or POD modes of the flow. Secondly, the Navier–Stokes equations tailored for the current flow are projected onto the POD modes using the Galerkin projection method to obtain the flow model, which consists of a set of nonlinear ordinary differential equations. These equations govern the time evolution of the POD modes. In the third and final step, stochastic estimation is used to correlate the flow velocity field to surface pressure data and to provide real-time updates of the state of the model derived in the previous step. Each of these three steps is discussed briefly in this section while additional essential steps in the derivation processes are given in the Appendix.

### 3.1. *Proper orthogonal decomposition technique*

The POD method was introduced to the fluid dynamics community by Lumley (1967) as an objective tool to extract information on the nature of energy-containing large-scale structures in a turbulent flow. Implementation of the POD technique requires detailed temporal or spatial correlation data in the flow, which nowadays can readily be obtained using either numerical simulations or laser-based planar flow measurements. The original derivation, however, favoured time-resolved data over long durations at a few spatial locations (hot-wire type data, e.g. Glauser *et al.* 1999; Citriniti & George 2000). More details of the method can be found in Berkooz, Holmes & Lumley (1993), Holmes, Lumley & Berkooz (1996), and Delville, Cordier & Bonnet (1998). Two decades after its introduction, Sirovich (1987) extended the POD approach and developed the snapshot method, which favours spatially resolved, but time-uncorrelated snapshots of the flow field. Such data can be obtained using numerical simulations or advanced optical diagnostics such as particle image velocimetry or planar Doppler velocimetry. We are currently using PIV data with the snapshot method. A brief summary of this technique follows while details of the snapshot method and its application in the present context are given in the Appendix.

The POD method uses $M$ snapshots of the flow and casts the fluctuations in the flow in terms of $N < M$ spatial orthonormal modes or POD modes, $\varphi_i(\boldsymbol{x})$, and modal

coefficients for these modes, $\boldsymbol{a}_i(t)$. The POD expansion (3.1) represents fluctuations of the vector $\boldsymbol{q}(\boldsymbol{x}, t) = [u(\boldsymbol{x}, t), v(\boldsymbol{x}, t), c(\boldsymbol{x}, t)]$ in terms of the modes that contain the major portion of the kinetic energy in the flow.

$$\boldsymbol{q}'(\boldsymbol{x}, t) \cong \sum_{i=1}^{N} a_i(t)\boldsymbol{\varphi}_i(\boldsymbol{x}). \tag{3.1}$$

For each of the flow cases explored in this work, 1000 PIV snapshots of the flow field are acquired (Little, Debiasi & Samimy 2006). Each snapshot contains two components $u$ and $v$ of instantaneous velocity on the $(x, y)$-plane passing through the centre of the cavity and the corresponding value for the speed of sound $c$ is calculated based on the flow stagnation temperature. The results indicate that the mean turbulence kinetic energy converges after approximately 700 snapshots (Caraballo *et al.* 2006). To ensure convergence, all 1000 snapshots for each data set were used to obtain the POD modes.

The PIV images are used to derive five different reduced-order models for the design and implementation of feedback control in the experiments. One model uses 1000 snapshots from the baseline (unforced) Mach 0.3 flow and each of the other four models uses 1000 snapshots from the baseline flow combined with 1000 snapshots from various open-loop forced Mach 0.3 flows exhibiting very different characteristics. The motivation for these combinations is to make the model as rich as possible within the constraint of using only a few modes (four in the current case) for its construction.

### 3.2. *Galerkin projection*

The second step in the process of deriving a reduced-order model is the projection of the Navier–Stokes equations governing the flow onto the POD modes, $\boldsymbol{\varphi}_i(\boldsymbol{x})$, using the Galerkin projection method. Starting from the compressible Navier–Stokes equations derived in Rowley (2002), this procedure produces a set of nonlinear ordinary differential equations for the modal coefficients $\boldsymbol{a}(t) = [a_1(t)a_2(t)\ldots a_N(t)]$ in (3.1). More details on the projection procedure are given in the Appendix.

Each flow variable is initially decomposed, using Reynolds decomposition, into its mean and fluctuating components. Then, the POD expansion (3.1) is written for each of the fluctuating components. Finally, the flow variables in the Navier–Stokes equations are replaced by the expanded expressions of mean and fluctuating components. The new form of the governing equations is then projected onto the POD modes by taking the inner product of each term with the POD modes according to the vector norm introduced in Rowley (2002). The resulting set of ordinary differential equations for the modal coefficients in (3.1), termed the Galerkin model (GM), has the form

$$\dot{\boldsymbol{a}}(t) = \boldsymbol{F} + \boldsymbol{G}\,\boldsymbol{a}(t) + \begin{bmatrix} \boldsymbol{a}^T(t)\boldsymbol{H}^1\boldsymbol{a}(t) \\ \vdots \\ \boldsymbol{a}^T(t)\boldsymbol{H}^N\boldsymbol{a}(t) \end{bmatrix}, \tag{3.2}$$

where $\boldsymbol{F}$, $\boldsymbol{G}$ and $\boldsymbol{H}^i$, $i = 1, \ldots, N$, are constant coefficient matrices obtained from the Galerkin projection. The number of modes used in the POD description of the flow, $N$, defines the number of equations.

The GM (3.2) is autonomous (i.e. the control input is implicit in the equations and is not clearly identified) and not useful for controller design. A few different methods are currently being explored to derive a model where the control input appears explicitly in the equations. The method used in the present work is based on spatial subdomain separation, which yields a new GM expressed by the following set

of ordinary differential equations

$$\dot{\boldsymbol{a}}(t) = \boldsymbol{F} + \boldsymbol{G}\boldsymbol{a}(t) + \begin{bmatrix} \boldsymbol{a}^T(t)\boldsymbol{H}^1\boldsymbol{a}(t) \\ \vdots \\ \boldsymbol{a}^T(t)\boldsymbol{H}^N\boldsymbol{a}(t) \end{bmatrix} + \boldsymbol{B}\Gamma(t) + \begin{bmatrix} (\bar{\boldsymbol{B}}^1\Gamma(t))^T\boldsymbol{a}(t) \\ \vdots \\ (\bar{\boldsymbol{B}}^N\Gamma(t))^T\boldsymbol{a}(t) \end{bmatrix}, \tag{3.3}$$

where the matrices of constant coefficients $\boldsymbol{F}$, $\boldsymbol{G}$, $\boldsymbol{H}^i$, $\boldsymbol{B}$ and $\bar{\boldsymbol{B}}^i$, $i = 1, \ldots, N$, are obtained from the Galerkin projection, and $\Gamma(t)$ is the control input applied at the forcing location. The GM (3.3) represents a reduced-order model of the cavity flow in terms of the control input, $\Gamma(t)$, and the modal coefficients, $\boldsymbol{a}_i(t)$, obtained with the POD method from $M$ time-uncorrelated PIV snapshots.

Using a finite number $N$ of modes to describe the flow, not only filters out smaller flow structures, but also does not account for the energy transfer process between the $N$ retained modes and all the neglected modes. Therefore, an additional viscous term, the modal eddy viscosity (Noack, Tadmor & Morzynski 2004), is added to maintain the overall energy balance and to compensate for the truncated modes. The additional viscosity is obtained by a modal energy balance (Noack *et al.* 2004) and added to the viscous term in the Navier–Stokes equations.

### 3.3. *Stochastic estimation*

The design of a controller based on the reduced-order model (3.3) will be presented and discussed in §5. For experimental implementation of the controller, the variables of the model must be linked to flow variables that can be measured experimentally in real-time. A similar need will arise in any practical application as well. In most systems, real-time experimental measurements can be obtained only via surface pressure or surface shear stress measurements. We use the stochastic estimation method for correlating the model variables to surface pressure measurements. Stochastic estimation (SE) was originally proposed and used by Adrian (1979) as a means of extracting coherent structures from a turbulent flow field. The technique estimates flow variables at any location by using statistical information about the flow at a limited number, $\mathscr{L}$, of locations. The method has been used to study flow structures in various flows (e.g. Adrian & Moin 1988; Cole & Glauser 1998), and as a tool in POD modelling to estimate the modal coefficients from experimental measurements in subsonic jets (Picard & Delville 2000) and in cavity flows (Samimy *et al.* 2004; Ukeiley & Murray 2005). It has also been used to estimate the modal coefficient of POD models for feedback flow control (e.g. Glauser *et al.* 2004; Siegel *et al.* 2005; Caraballo *et al.* 2005, 2006).

In the current work, quadratic stochastic estimation is employed to estimate the modal coefficients of the flow model (3.3) directly from real-time measurements of surface pressure fluctuations at a small number, $\mathscr{L}$, of locations. The estimates of the modal coefficients can be written in the following form

$$\hat{a}_i(t) = C^{ij}p'_j(t) + D^{ijk}p'_j(t)p'_k(t) \qquad (i = 1, \ldots, N, \qquad k, l, \ldots = 1, \ldots, \mathscr{L}), \tag{3.4}$$

where $\boldsymbol{C}$ and $\boldsymbol{D}$ are the matrices of the estimation coefficients found by minimizing the average mean square error, $e_i$, between the values of $a_i(t_r)$ obtained by projecting the velocity fluctuations from the snapshots onto the POD basis

$$a_i(t_r) = \int_s \boldsymbol{q}'(\boldsymbol{x}, t_r)\boldsymbol{\varphi}_i(\boldsymbol{x})\,\mathrm{d}\boldsymbol{x} \qquad (r = 1, \ldots, M), \tag{3.5}$$

and the estimated ones $\hat{a}_i(t_r)$ from (3.4) at the same times.

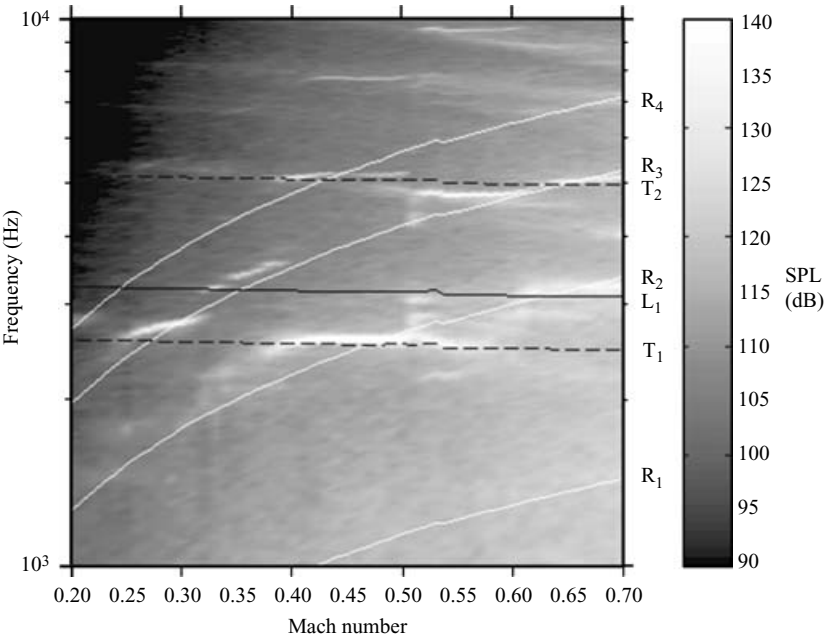


FIGURE 3. Spectral characteristics of cavity for various Mach numbers measured with transducer 8 located in the middle of the cavity floor.

To calculate the matrices in the SE (3.4), we use surface pressure measurements at the $\mathscr{L} = 6$ locations in the cavity wall (sensors 1–6 in figure 2) taken simultaneously with the PIV snapshots. A total of 1000 simultaneous PIV-surface pressure measurements are acquired for each flow case. Whereas linear stochastic estimation has often been used in the literature, Naguib, Wark & Juckenhoefel (2001) used both linear and quadratic terms for an accurate estimate of the flow field from wall surface pressure measurements. For the cavity flow, this was confirmed by Murray & Ukeiley (2002) and by Caraballo *et al.* (2004). Similar observations were presented by Ausseur *et al.* (2006) for the case of flow separation control. Both the linear and the quadratic terms of (3.4) are retained in the current work as well. The stochastic estimation process is repeated for each model based on the individual and combined sets of snapshots discussed in this work.

The flow characteristics for the baseline and the open-loop forced cases along with the characteristics for several reduced-order models are presented and discussed in the next section. This is followed by the control design and implementation in § 5 and presentation and discussion of the results in controlled flows in § 6.

## 4. Flow characteristics and reduced-order model results

### 4.1. *Flow and surface pressure characteristics*

The cavity depth in the experiment is adjustable, but only a depth of 12.7 mm (0.5 in) corresponding to an aspect ratio, $L/D$, of 4 is used for all the results reported in this work. In order to characterize the coupling between the acoustic and the flow fields, we initially surveyed the flow between Mach numbers 0.2 and 0.7 with an increment of 0.01. For each of these cases, dynamic surface pressure measurements were obtained using transducer 8 at the centre of the cavity floor (figure 2). Figure 3 summarizes

| Case | Forcing frequency (Hz) | Comments |
|---|---|---|
| B | – | Baseline flow |
| F1 | 1610 | Open-loop forcing |
| F2 | 1830 | Open-loop forcing |
| F3 | 3250 | Open-loop forcing |
| F4 | 3920 | Open-loop forcing |
| MB | – | Control model based on B snapshots |
| MBF1 | – | Control model based on B and F1 snapshots |
| MBF2 | – | Control model based on B and F2 snapshots |
| MBF3 | – | Control model based on B and F3 snapshots |
| MBF4 | – | Control model based on B and F4 snapshots |

TABLE 1. Mach 0.3 flow baseline and open-loop forced flows and the models.

the results by showing the SPL amplitude and frequency as a function of the Mach number. Also shown are the lines corresponding to the first four Rossiter modes (R1–R4) predicted by the modified Rossiter formula (Heller & Bliss 1975), the first longitudinal acoustic mode based on the cavity length (L1), and the first and second transversal acoustic modes based on tunnel height (T1, T2). Strong resonant tones are observed near the intersections of the predicted Rossiter modes with both the transversal and the longitudinal acoustic modes. The observation of the interaction between Rossiter and transversal acoustic modes is similar to that of Ziada *et al.* (2003) who explored low subsonic cavity flows. The work of Rossiter (1964), Rockwell & Naudascher (1978) and Williams *et al.* (2000) all examined cavity flows for which the tunnel vertical dimension was significantly larger than the cavity length. In these cases, only the interaction of Rossiter modes with the longitudinal cavity acoustic mode was observed.

Based on these observations and other similar results (Debiasi & Samimy 2004), we use Mach 0.3 flow as our reference baseline case because it shows a single tone at about 2850 Hz, which is near the intersection of the third Rossiter mode and the first transversal acoustic mode at 2700 Hz. At this Mach number, the actuator has sufficient authority to significantly alter the flow and real-time feedback control can be readily implemented. Table 1 gives the baseline and the four open-loop forced flows as well as control models explored in the current work.

For the B (baseline) Mach 0.3 cavity flow case, figure 4(*a*) presents the SPL spectrogram, and figure 4(*b*) the corresponding spectrum of the surface pressure measured by transducer 5, from figure 2. Measurements from the other transducers, not shown here, provide consistent results, confirming that at this Mach number, the cavity flow resonates at a frequency corresponding to the third Rossiter mode with strong time-invariant flow-acoustic coupling. At other Mach numbers, the cavity oscillations can exhibit rapid switching between multiple modes creating a distribution of energy over a variety of frequencies.

Figure 5 shows the effect of open-loop forcing, cases F1–F4, in which the resonant peak in the baseline case is significantly reduced and other modes have appeared. Figure 5(*a*) shows the effect of actuation at 1610 Hz, for which the peak is reduced by almost 20 dB with the introduction of a small peak at the forcing frequency. The forcing peak was more pronounced at the locations of transducers 4 and 6, indicating significant pressure variations within the cavity for this case. Figure 5(*b*) illustrates the effect of forcing at 1830 Hz, the frequency corresponding to the second Rossiter mode for this flow (figure 3). This forcing disrupts the natural resonance

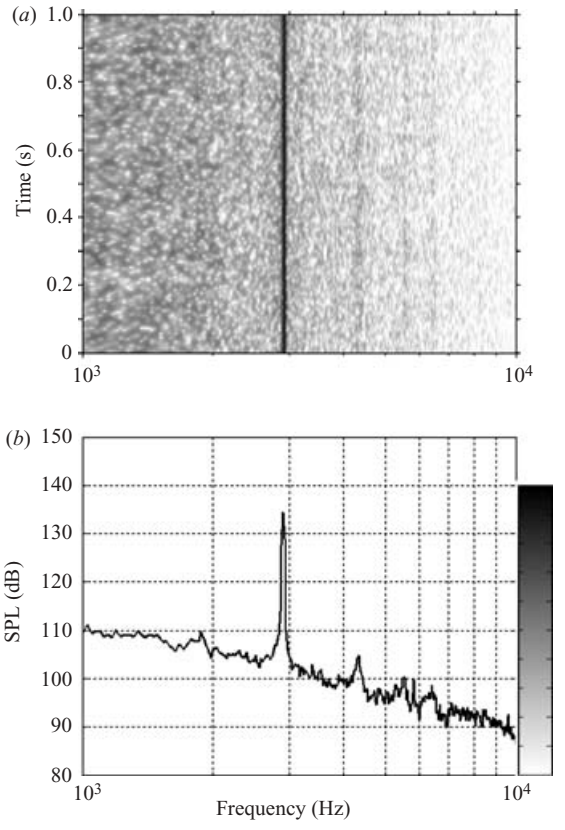


FIGURE 4. (*a*) SPL spectrogram and (*b*) spectrum of baseline Mach 0.3 cavity flow (case B) from transducer 5.

and artificially induces a resonance congruous with the second Rossiter mode. The corresponding spectrogram shows that the peak induced by forcing is time-invariant, which is typical for single-mode resonance. Consistent results were obtained from the other transducers in the test-section wall.

Figure 5(*c*) illustrates the effect of forcing at 3250 Hz, one of the optimal forcing frequencies discussed by Debiasi & Samimy (2004). This case artificially induces a multi-mode state in the flow with rapid switching between the resonant and control frequencies and a consequent spreading of the pressure fluctuations. Similar results were obtained from the other transducers in the test-section wall. It should be noted that, because of the subtle geometry change introduced by the laser exhaust slot in the cavity floor, the effect of the forcing presented here differs slightly form that reported in Debiasi & Samimy (2004). Figure 5(*d*) shows the effect of forcing at 3920 Hz (near the fourth Rossiter mode, figure 3), another optimal sinusoidal forcing which significantly reduces the resonant peak. The forcing induces a peak at its subharmonic (close to the second Rossiter mode) that competes with the baseline resonant frequency on a rapid time scale, thus inducing a multi-mode state. Consistent results were obtained from the other transducers in the test-section wall.

Figure 6 presents the instantaneous and phase-averaged (over 50 images) planar flow-visualization images and of the B, F2 and F4 cases. Three coherent large-scale structures are clearly visible in the B case (figure 6*a*, *b*) consistent with the cavity flow

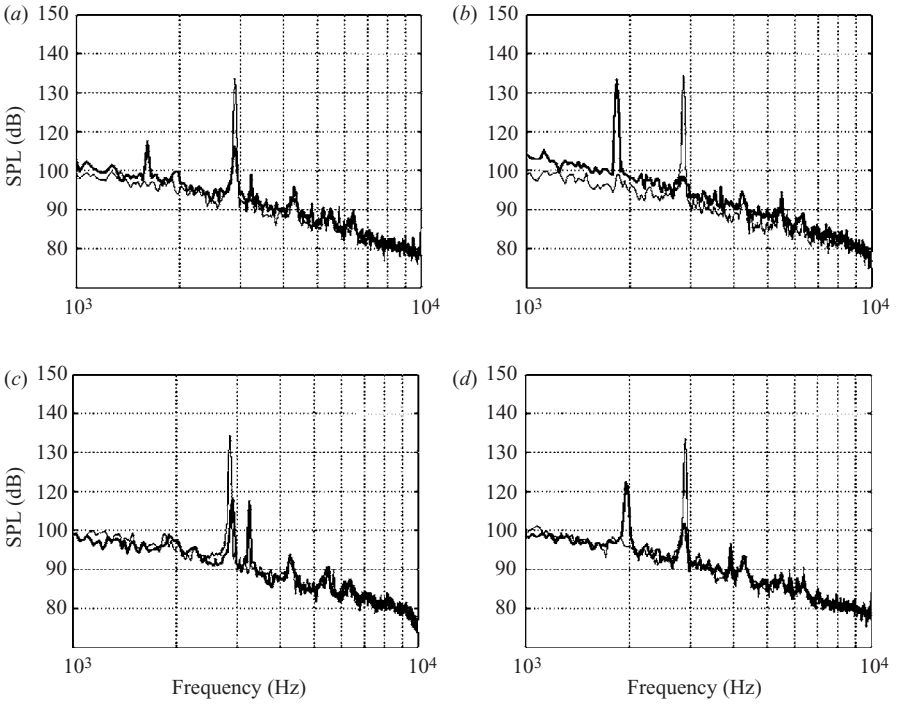


FIGURE 5. SPL spectra from transducer 5 for Mach 0.3 cavity flow. The thin line is the B case and the thick line is with open-loop forcing at cases: (*a*) F1; (*b*) F2; (*c*) F3; (*d*) F4.

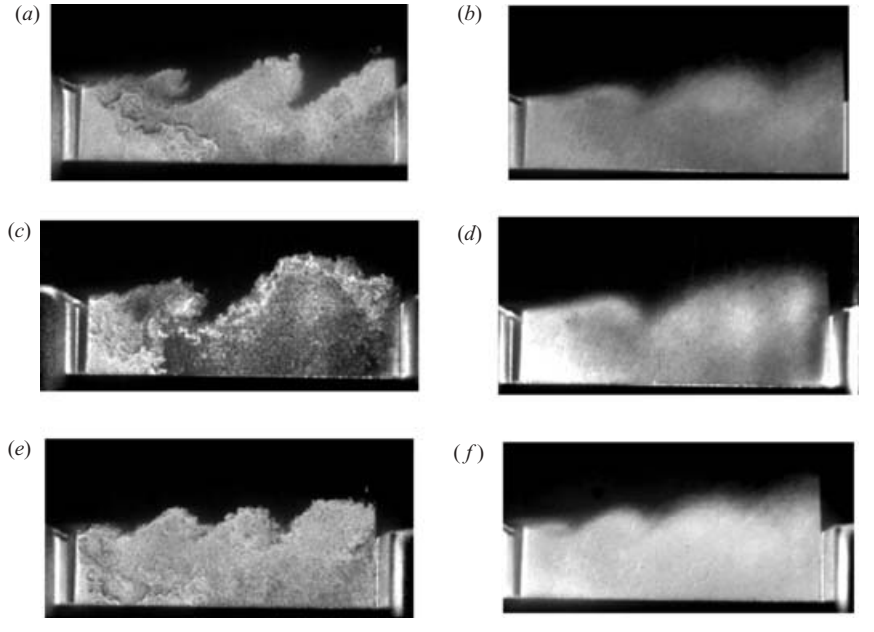


FIGURE 6. Instantaneous (*a*, *c*, *e*) and phase-averaged (*b*, *d*, *f*) planar flow-visualization images of the cavity flow for: (*a*, *b*) B; (*c*, *d*) F2; (*e*, *f*) F4. Flow is from left to right and the leading and trailing edges of the cavity are shown in the flow-visualization images.

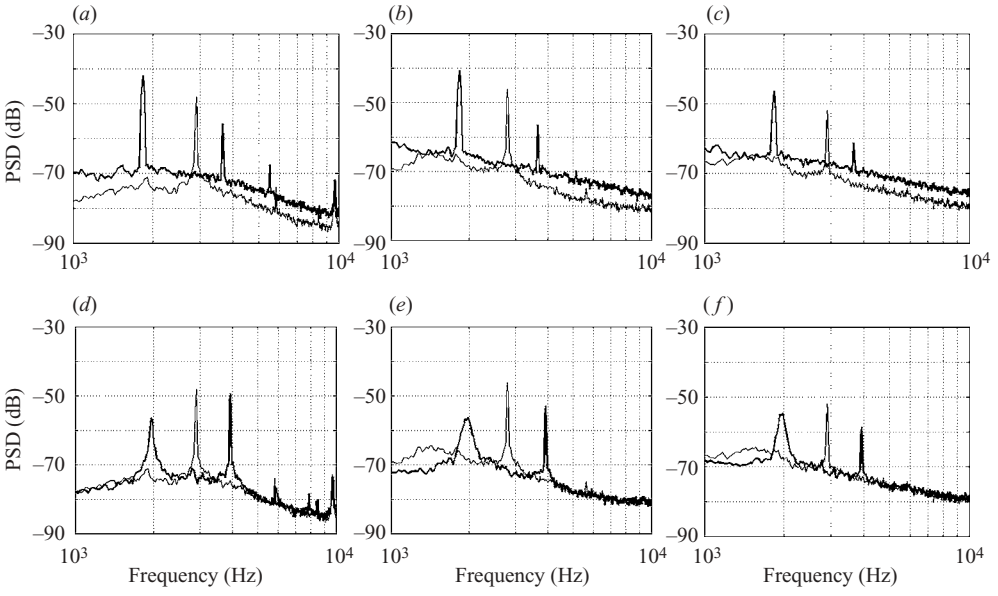


FIGURE 7. Velocity spectra from hot-wire measurements of Mach 0.3 cavity flow at three streamwise locations ($x/D = 1, 2, 3$; from left to right). The thin line is the B case and the thick line is for open-loop forcing cases: ($a$–$c$) F2 and ($d$–$f$) F4.

resonance at the third Rossiter mode for this baseline flow. Images in figure 6($c$, $d$) are for the F2 case (excitation at the second Rossiter mode frequency) for which, as expected, two large coherent structures are clearly visible in the shear layer. This visually confirms that forcing at this frequency eliminates or drastically weakens the natural feedback mechanism for the third Rossiter mode, but excites the flow at the lower resonant frequency (figure 5$b$). Images in figure 6($e$, $f$) present the F4 case. Four large-scale structures are visible in the instantaneous image of the flow for this forcing near the fourth Rossiter mode whereas the average data exhibit discrete structures in the upstream half of the cavity, but less-defined large-scale dynamics along the downstream half. Phase-averaged fluctuating normal velocity components obtained using PIV show results consistent with these images, confirming the existence of three, two and four structures in B, F2 and F4 cases, respectively (Little, Debiasi & Samimy 2006).

To obtain a more quantitative description of the frequency content of cavity shear-layer structures, a hot-wire survey at three streamwise locations was performed. The velocity spectra shown in figure 7 correspond to the cases of figure 6, where the two open-loop forcing cases (F2 and F4) have been superimposed on the baseline case (B) to allow easier comparison. The strong resonance of case B (thin line) is exhibited by the peak at the third Rossiter mode that remains dominant over the length of the cavity, consistent with the flow-visualization images in figure 6($a$, $b$). As $x/D$ increases, higher broadband energy levels are also observed. This is due to an increase in turbulence intensity and the extended scale of turbulence, as large-scale structures advect in the shear layer of the cavity and entrain more fluid from both sides of the shear layer. Similar behaviour is shown for case F2 (figure 7$a$–$c$), albeit at a lower frequency. Consistent with the visualization of figure 6($c$, $d$), the flow is now resonating at the second Rossiter mode which remains dominant over the cavity

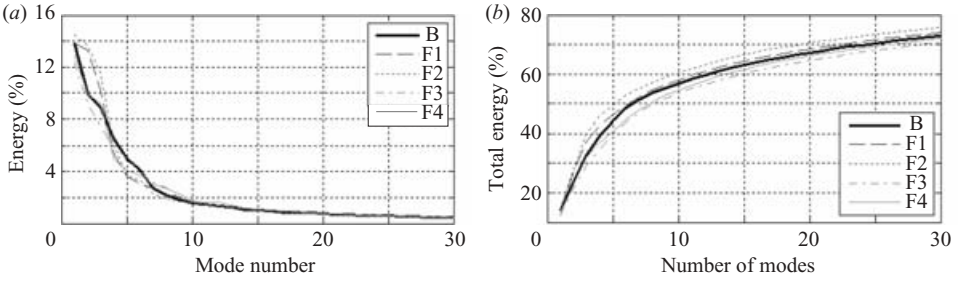


FIGURE 8. Energy content of the first 30 POD modes (*a*) and cumulative energy of the modes (*b*) for the v-component of velocity fluctuations of the baseline flow and the four open-loop forced flows.

length surveyed. As with case B, increases in broadband levels are observed with increases in $x/D$. An indication of strong flow-acoustic coupling is observed when comparing the SPL spectra of figure 5 with the velocity spectra of figure 7. For case B, flow and surface pressure both show resonance at the same frequency, the third Rossiter mode, while for F2, the flow and surface pressure show resonance primarily at the second Rossiter mode. One difference between the velocity spectra of cases B and F2 and their respective flow–acoustic coupling mechanisms is the existence of harmonics in the flow for the F2 case. No harmonics are observed in the F2 SPL spectrum, implying that these frequencies do not contribute significantly to flow–acoustic coupling.

The velocity spectra for F4 (figure 7*d–f*) show examples of multi-mode resonance where the flow energy is now shared between the forcing frequency (fourth Rossiter mode) and its broadened subharmonic near the second Rossiter mode. In addition, as $x/D$ increases, the broadened subharmonic actually becomes slightly dominant over the control frequency. It is believed that this behaviour is an indication of structure pairing or merging events that occur over the latter half of the cavity, a possible explanation for the less coherent behaviour observed in the downstream portion of figure 6(*e*, *f*). This suggests that one strategy for successful cavity flow control is to excite oscillations at competitive or non-resonant frequencies, thereby not supplying sufficient energy or permitting the necessary feedback to allow selective amplification over the extent of the cavity length. However, we have seen that a sufficient increase in the actuation amplitude (not shown) allows both the velocity and surface pressure spectra to become dominantly resonant at the fourth Rossiter mode, similar to the F2 case. Accordingly, we have to balance both frequency and to a lesser degree excitation amplitude when applying open-loop control (Debiasi & Samimy 2004). As expected, the SPL spectrum of this flow (figure 5*d*) also exhibits multi-mode behaviour where the energy is distributed between various modes with the second Rossiter mode containing the most energy. As in the velocity spectra for B and F2, increases in broadband energy levels are observed corresponding to increases in $x/D$. Velocity spectra for remaining open-loop forcing cases, F1 and F3 (not shown) display similar behaviour to those in figure 7 where F1 behaves like F2 (dominant peak at the forcing frequency) and F3 behaves similarly to F4 (multi-mode fluidic resonance).

The results presented above clearly confirm the authority of the actuator at this Mach number and the ability of the experimental set-up to alter the flow significantly in a controlled fashion.

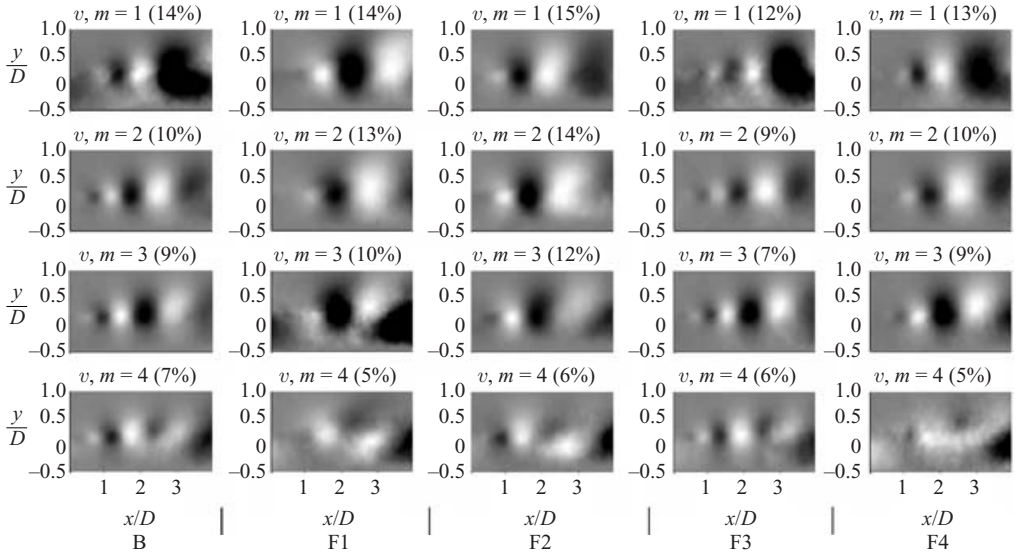


FIGURE 9. The first four POD modes for the $v$-component of velocity fluctuations of the baseline flow and the four open-loop forced flows.

### 4.2. *Reduced-order modelling results*

Figure 8 shows the energy distribution of the first 30 POD modes for the baseline and each of the open-loop forced cases. It can be seen that more energy is recovered by modes 1–3 in the F1and F2 cases, i.e. in flows with larger, more organized shear-layer structures. In terms of cumulative modal energy (figure 8*b*), the larger energy recovery of these modes is not compensated by the lower recovery of the successive modes 4–6. This is particularly visible for F2. Conversely, cases F3 and F4, characterized by smaller and less organized structures, exhibit a smaller lower mode energy recovery. The energy recovery of all the successive modes appears to be similar for all the cases.

Figure 9 shows the first four POD modes of the $v$-component of velocity fluctuations for the baseline flow (B) and each of the four open-loop forced flows (F1–F4). For the B case, all four modes show three structures in the flow, consistent with the cavity resonance at the third Rossiter mode (figures 3 and 6*a–c*). These four modes contain about 40 % of the energy in the $v$-component. The POD modes shown for B and F2 in figure 9 show a structure pattern similar to the phase-averaged $v$-component of velocity fluctuations from PIV data (Little *et al.* 2006). In order to keep the reduced-order model tractable and also amenable to controller design and implementation, only these four modes are used in the design of the controller.

In F1 and F2, the flow is forced at frequencies close to or coincident with the second Rossiter mode. Accordingly, two structures are present in the modes congruent with figures 3 and 6(*d–f*). For both cases, the first four modes contain about 45 % of the energy. When forced at 3250 Hz (F3) the flow has modal behaviour similar to case B, with the presence of three structures. However, the structures have smaller size. The subharmonic of the forcing frequency in case F4 is close to the second Rossiter mode and dominates the SPL spectrum (figure 5*d*). The first three POD modes for this case show the presence of two clearly defined structures, whereas the fourth mode exhibits a more smeared pattern, congruent with the PIV data close to the cavity trailing edge. Thus, in contrast with flow visualization and PIV images (figure 6*e*, *f*), POD

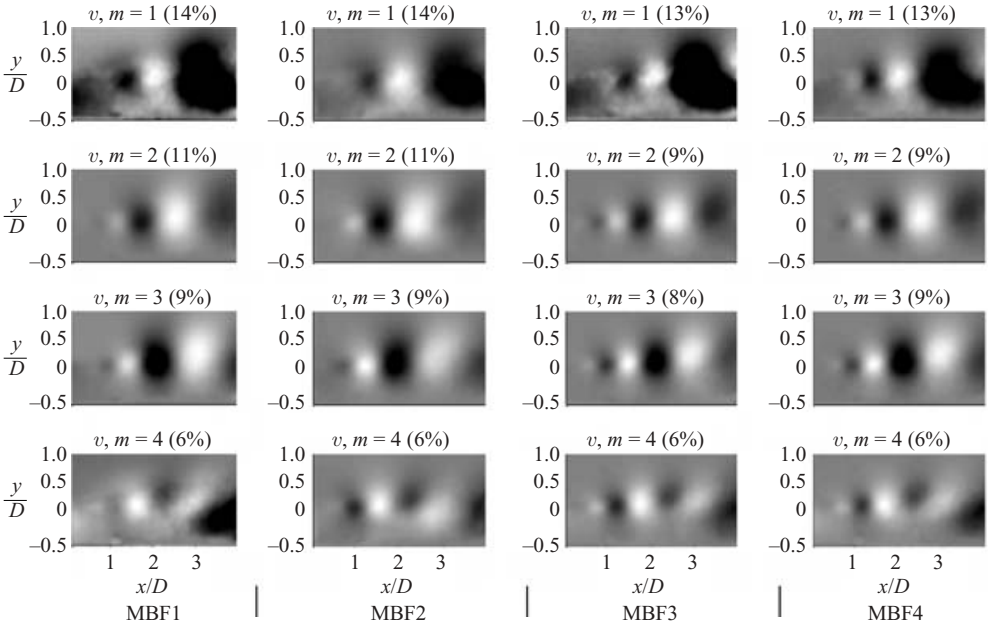


FIGURE 10. The first four POD modes for the $v$-component of velocity fluctuations for the combination of the baseline and the four open-loop forced flows.

modes seem biased toward capturing the flow subharmonic oscillations rather than the corresponding fundamentals. The energy contained in these four modes is about 37 %, lower than that of the baseline case.

Figure 10 shows the first four POD modes for the cases MBF1–MBF4, where the baseline is combined with one of the open-loop forced cases. The POD modes from the combined PIV snapshots take, as expected, some characteristics from each of the participating flows. For example, for the case MBF4 based on the combination of the B and F4 cases, the first and second modes contain two dominant structures as in F4, whereas the third and fourth modes contain three structures which resemble those of the B case. The combined data sets for the snapshots are limited to two flow conditions only (baseline and one forced case) for consistency with the very low order ($N = 4$) chosen for the POD expansion. The incorporation of snapshots from multiple flow conditions beyond the two considered here would require a higher-order dynamical system (3.3) to capture the various characteristics of the flow exhibited by different flow conditions. Although it is possible in principle to increase the order of the POD expansion, this comes at the expense of a more complicated state space model for control design, which would also require a larger number of independent pressure measurements for state estimation.

The reduced-order model, (3.3), obtained by Galerkin projection of the Navier–Stokes equations onto the POD modes, is solved to check the time evolution of the modal coefficients which, with $N = 4$, converge for the all five models in table 1. Figure 11 shows the evolution of the first modal coefficient of the MB and the MBF4 cases. As expected, after an initial transient period, the modal coefficients oscillate in a bounded fashion around zero. The thick lines in these figures represent the limits of 2 standard deviations of the corresponding modal coefficients obtained using (3.5) from the PIV snapshots. This allows a qualitative validation of (3.3) which indicates that its

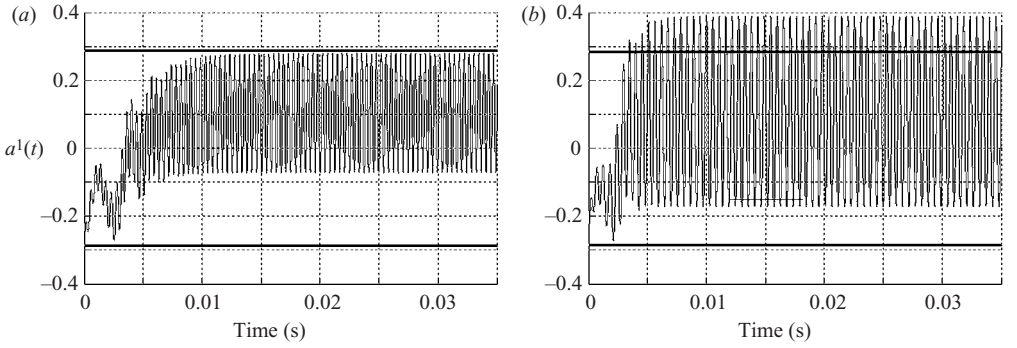


FIGURE 11. The first POD modal coefficient in the Galerkin system from (3.3) for two different models: (*a*) MB; (*b*) MBF4. The thick horizontal lines correspond to two standard deviations of modal coefficients obtained from PIV snapshots and (3.5).

solutions fall within or close to the range obtained from the PIV measurements. The system trajectories converge to the same values irrespective of the modal coefficient used as the initial condition for the solution of the reduced-order model (3.3). This implies the existence of a stable limit cycle. Similar results are obtained for the modal coefficients of the other three cases. We have also shown previously that the modal coefficients obtained with (3.4) compare well with those obtained from PIV snapshots using (3.5) (Caraballo *et al.* 2005, 2006).

## 5. Controller design and implementation

In this section, we present and discuss the methodology for the design of the reduced-order model based controller. The procedure includes equilibrium computation, coordinate transformation, linear approximation of the Galerkin system, and linear-quadratic state-feedback control design. In this work, we have considered the five reduced-order flow models MB and MBF1–MBF4, obtained as described in the previous sections and summarized in table 1. The expression for the reduced-order flow model for all five cases is the same nonlinear state space model given by (3.3), with $N = 4$, whereas the numerical values of the model parameters vary for each case.

### 5.1. *Equilibrium analysis and model simplification*

The first step in the design of a feedback control law is to shift the origin of the coordinate system of the reduced-order model (3.3) to the equilibrium point, $\boldsymbol{a}_0$. To accomplish this goal, a Newton iterative algorithm has been implemented to compute the equilibrium point for the unforced system (3.2) (Yuan *et al.* 2005). Shifting the origin of (3.3) to the equilibrium point, removes the constant terms in the equations. The resulting simplified state space model in the new set of coordinates $\tilde{\boldsymbol{a}} = \boldsymbol{a} - \boldsymbol{a}_0$ describing the behaviour of the system around the equilibrium point becomes

$$\dot{\tilde{\boldsymbol{a}}} = \tilde{\boldsymbol{G}}\tilde{\boldsymbol{a}} + \begin{bmatrix} \tilde{\boldsymbol{a}}^T H^1 \tilde{\boldsymbol{a}} \\ \vdots \\ \tilde{\boldsymbol{a}}^T H^4 \tilde{\boldsymbol{a}} \end{bmatrix} + \tilde{\boldsymbol{B}}\Gamma + \begin{bmatrix} (\bar{\boldsymbol{B}}^1 \Gamma)^T \tilde{\boldsymbol{a}} \\ \vdots \\ (\bar{\boldsymbol{B}}^4 \Gamma)^T \tilde{\boldsymbol{a}} \end{bmatrix}, \tag{5.1}$$

| Model | Open loop eigenvalues | |
|---|---|---|
| MB | $\lambda_{1,2} = 1597 \pm 7023\mathrm{i}$ | $\lambda_3 = -3652, \quad \lambda_4 = -880$ |
| MBF1 | $\lambda_{1,2} = 270 \pm 6491\mathrm{i}$ | $\lambda_3 = -1847, \quad \lambda_4 = -623$ |
| MBF2 | $\lambda_{1,2} = 433 \pm 12458\mathrm{i}$ | $\lambda_{3,4} = -397 \pm 1779\mathrm{i}$ |
| MBF3 | $\lambda_{1,2} = -1492.6 \pm 7532\mathrm{i}$ | $\lambda_3 = -2742, \quad \lambda_4 = -674$ |
| MBF4 | $\lambda_{1,2} = 1397 \pm 7062\mathrm{i}$ | $\lambda_3 = -2871, \quad \lambda_4 = -697$ |

TABLE 2. Eigenvalues of the open-loop system for each model.

where

$$\tilde{\boldsymbol{G}} = \boldsymbol{G} + \begin{bmatrix} \boldsymbol{a}_0^T(\boldsymbol{H}^1 + (\boldsymbol{H}^1)^T) \\ \vdots \\ \boldsymbol{a}_0^T(\boldsymbol{H}^4 + (\boldsymbol{H}^4)^T) \end{bmatrix}, \quad \tilde{\boldsymbol{B}} = \boldsymbol{B} + \begin{bmatrix} (\bar{\boldsymbol{B}}^1)^T \boldsymbol{a}_0 \\ \vdots \\ (\bar{\boldsymbol{B}}^4)^T \boldsymbol{a}_0 \end{bmatrix}.$$

Clearly, the adapted model has an equilibrium point at the origin, which is more convenient for controller design and stability analysis.

### 5.2. *Linear quadratic state feedback control*

To apply linear control design, a linear approximation of (5.1) at the origin is readily obtained as

$$\dot{\tilde{\boldsymbol{a}}} = \tilde{\boldsymbol{G}}\tilde{\boldsymbol{a}} + \tilde{\boldsymbol{B}}\Gamma. \tag{5.2}$$

The eigenvalues of the system matrix $\tilde{\boldsymbol{G}}$ computed for each of the five models are given in table 2.

It can be seen from table 2 that the models exhibit the same qualitative features in the linear approximation, as the open-loop matrices possess two unstable complex conjugate eigenvalues and two stable eigenvalues. The presence of two unstable complex conjugate eigenvalues implies, as expected, that the flow corresponding to the equilibrium, $\boldsymbol{a}_0$, is an unstable solution for the GM (3.2). Since the pairs, $(\tilde{\boldsymbol{G}}, \tilde{\boldsymbol{B}})$, for all five cases are controllable, linear state-feedback design based on the linearized model (5.2) offers a simple approach to the design of a controller for the nonlinear model (5.1). Recall that the stochastic estimation method provides a way to estimate the modal coefficients of the GM from real-time surface pressure measurements with (3.4). The availability of real-time estimates of the state of the GM (5.1) allows the use of linear state-feedback control to globally stabilize the origin of (5.2). This, in turn, yields a controller that locally stabilizes the origin of the nonlinear system (5.1).

A convenient and well-established methodology for the state-feedback controller design is offered by linear-quadratic (LQ) optimal control. The LQ design computes the gain matrix, $\boldsymbol{K}$, such that the state-feedback law

$$\Gamma(t) = -\boldsymbol{K}\tilde{\boldsymbol{a}}(t), \tag{5.3}$$

minimizes the quadratic cost function

$$J_c(\tilde{\boldsymbol{a}}, \Gamma) = \int_0^\infty (\tilde{\boldsymbol{a}}^T W_{\tilde{\boldsymbol{a}}} \tilde{\boldsymbol{a}} + W_\Gamma \Gamma^2)\, \mathrm{d}t, \tag{5.4}$$

where $W_{\tilde{\boldsymbol{a}}} > 0$ and $W_\Gamma > 0$ are positive definite weighting functions for the state vector and the control signal, respectively. Minimization of $J_c$ results in asymptotic stabilization of the origin, while keeping the control energy small. In our design, the weights have been chosen as $W_{\tilde{\boldsymbol{a}}} = I_{4\times4}$ and $W_\Gamma = 1$ for all the models. For the

| Model | Controller gain $K$ | $\alpha$ |
|---|---|---|
| MB | [−56 8.8 −417 −12.8] | 0.265 |
| MBF1 | [2.6 −19.9 −27.0 −16.1] | 1 |
| MBF2 | [1.7 69.5 36.3 −33] | 0.62 |
| MBF3 | [51.9 50.8 −320 −261] | 0.25 |
| MBF4 | [17.6 209 11.6 −147] | 0.5 |

TABLE 3. Controller gains.

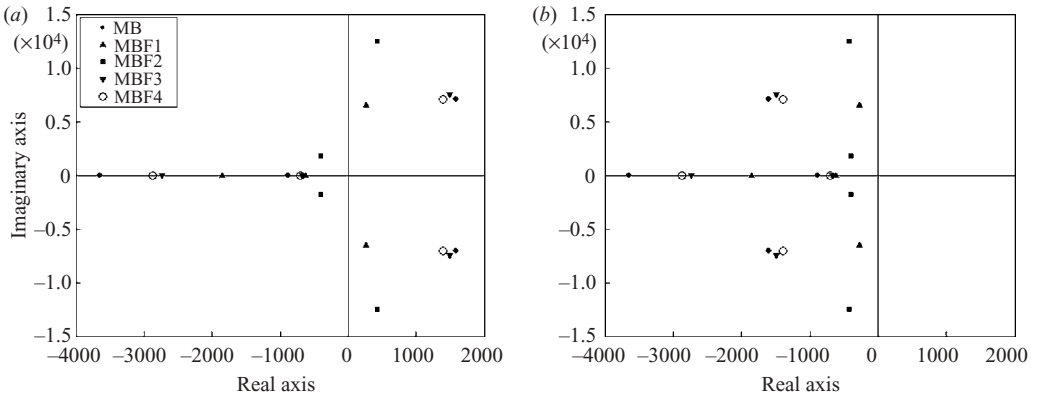


FIGURE 12. Eigenvalues of (*a*) the open-loop system and (*b*) the closed-loop system for each model.

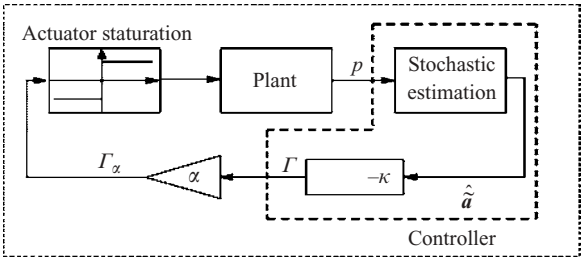


FIGURE 13. Diagram of the closed-loop system with LQ state-feedback control.

particular system under consideration, it has been observed that increasing the control weight, $W_\Gamma$, with respect to $W_{\tilde{a}}$ has little effect on the location of the closed-loop eigenvalues. As a result, the simplest possible choice of the weighting functions that ensures closed-loop stability has been adopted. The corresponding control gains for each model are given in table 3.

It is well known that applying LQ state-feedback control (5.3) to the linearized system (5.2) results in mirroring all the right-hand half-plane eigenvalues of the matrix $\tilde{G}$ to the left-hand half-plane, while the left-hand half-plane eigenvalues remain practically unchanged (figure 12). Results of nonlinear simulations of the closed-loop system (5.1)–(5.3) show that the trajectory of $\boldsymbol{a}(t)$ converges to the corresponding equilibrium point, $\boldsymbol{a}_0$, in each of the considered cases. This indicates that, at least in principle, the LQ controller designed for the linear approximation (5.2) succeeds in stabilizing the equilibrium of the four-dimensional nonlinear GM (5.1).

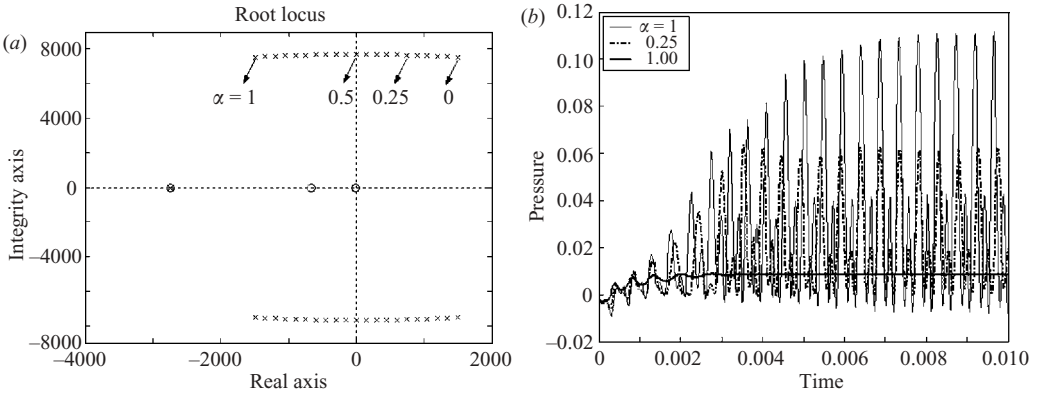


FIGURE 14. Simulation results of the closed-loop system with different scaling factor, $\alpha$, for MBF3 flow model: (*a*) root locus and (*b*) closed-loop responses at the location of transducer 3.

## 6. Real-time feedback control results and discussion

Before presenting the results of the experimental implementation of the controller, it is worth summarizing the structure of the reduced-order model-based controller derived in § 5. As depicted in figure 13, the controller includes a stochastic estimation subsystem and a feedback from the estimated states. The estimate, $\hat{\hat{\boldsymbol{a}}}$, of the deviation from the equilibrium of the modal coefficients of the GM, required to implement the feedback law (5.3), may, in principle, be obtained by means of stochastic estimation by first estimating $\hat{\boldsymbol{a}}(t)$ from raw pressure measurements using (3.4), and then subtracting the equilibrium value, $\boldsymbol{a}_0$, computed from the model data. However, in implementing the controller, subtracting the equilibrium values from the estimated modal coefficients is not necessary, since the DC component is removed from the pressure measurements by means of high-pass filtering. That is, the estimator (3.4) naturally produces the values of the zero-mean fluctuations, $\hat{\hat{\boldsymbol{a}}}$, from pressure measurements. It is also important to point out that, to prevent any damage to the actuator, the control input signal must be limited to the range $\pm 10$ V. Since the gains of the LQ control (table 3) are quite large, constant saturations of the actuator were observed during initial closed-loop experiments for most of the cases under investigation. Therefore, it was necessary to introduce a scaling factor, $0 < \alpha \leqslant 1$, in the state-feedback to keep the actuator below the saturation limit. The resulting scaled control is in the form

$$\Gamma_\alpha(t) = -\alpha \boldsymbol{K} \hat{\hat{\boldsymbol{a}}}(t). \tag{6.1}$$

The scaling factors for each model are given in table 3. The specific value of $\alpha$ for each controller has been chosen empirically as the highest such value that keeps the magnitude of the scaled control signal (6.1) within the given bound. The performance of the closed-loop systems obtained with the scaled LQ control (6.1) replacing (5.3) has been evaluated using simulation. Typical results obtained for MBF3 are shown in figure 14. Figure 14(*a*) shows that the closed-loop eigenvalues are moved to the left half-plane only when $\alpha > 0.5$. However, figure 14(*b*) shows that, though the scaled LQ control is not capable of asymptotically stabilizing the origin of the nonlinear model (3.2), as shown for the scaling factor of $\alpha = 0.25$, it nevertheless provides a significant reduction of the amplitude of the stable limit cycle. These results are in agreement with a mathematical analysis carried out on the nonlinear finite-dimensional GM, which predicts a reduction of the amplitude of the limit cycle corresponding to

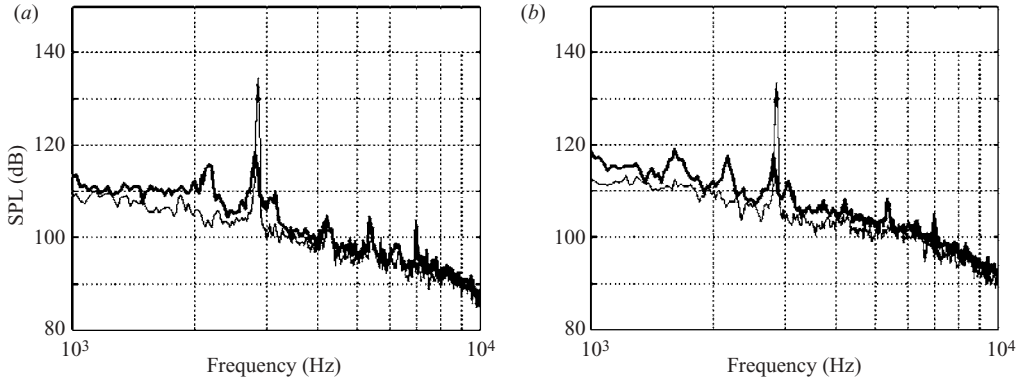


FIGURE 15. SPL spectra from transducer 5 and 6. The thin line is the B case and the thick line is control with LQ design based on the MB model: (*a*) sensor 5 and (*b*) sensor 6.

the fundamental cavity tone as the gain, $\alpha$, increases from 0 to 0.5, with complete suppression of the oscillation only possible for $\alpha > 0.5$. The results for the other models show similar trends. It must be kept in mind that stabilization of the origin of (5.1) corresponds to dissipation of the oscillations produced by the limit cycle, only as predicted by the simple model (5.1), which can capture the rich behaviour of the flow only in a limited qualitative sense. Therefore, when applying (6.1) to the experimental set-up, it must be expected that the pressure fluctuations are not completely suppressed, even when stabilization of (5.1) is achieved by the controller.

The performance of the control law (6.1) has been tested experimentally for different combinations of reduced-order models and flow conditions. In the following, we present and discuss the results obtained in controlling the baseline flow B. Since the goal of our controller is to reduce the amplitude of pressure oscillations, we use the SPL spectra as the primary measure of controller effectiveness. In general, spectra from each of the transducers of figure 2 are checked; however, we choose only to show the signal from transducer 5. If the results from the other transducers are significantly different, they are noted in the text. As an example of the relationship between sensors, we present surface pressure spectra from transducers 5 and 6 in figure 15 for the MB case. As expected, there are some differences in the data from the two sensors; however, the general trend of multi-mode resonance with no dominant peaks is conclusive. The MB-based LQ controller produces a considerable attenuation of the resonance peak and a redistribution of the energy into various modes.

The use of combined reduced-order models for cavity flow control is a relatively new topic and requires more work. Nevertheless, we present some preliminary results of these combinations that provide some insight into their control effect. When a model incorporating the baseline and one open-loop forcing case (figure 16) is considered in place of the MB model, the attenuation of the resonance tone is generally accompanied by the introduction of a new significant peak whose frequency is about 2000 Hz for MBF1 and MBF2 (figure 16*a*, *b*) and about 3200 Hz for MBF3 (figure 16*c*). The MBF4 case (figure 16*d*) is the most successful of the combined models as only a small peak, around 3200 Hz, is observed in the spectrum which exhibits multi-mode/peak splitting phenomena. In addition, we can compare the result obtained with the MB-based (figure 15*a*) and MBF4-based (figure 16*d*) LQ control to that obtained with the best open-loop forcing, F3 (figure 5*c*). In all cases, multi-mode behaviour has been induced in the cavity flow with attendant

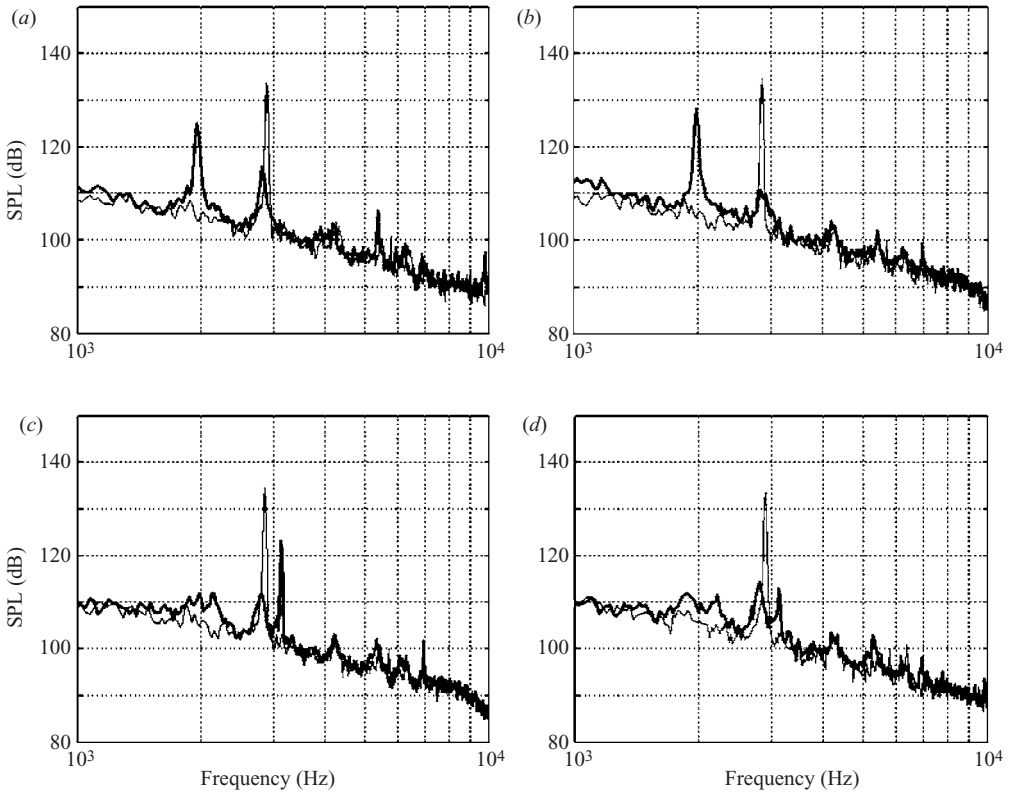


FIGURE 16. SPL spectra from transducer 5. The thin line is the B case and the thick line is control with LQ design based on the model: (*a*) MBF1; (*b*) MBF2; (*c*) MBF3; (*d*) MBF4.

spreading of the available pressure fluctuations at different frequencies. The MB and MBF4 closed-loop control cases perform better than the open-loop control since they produce slightly lower maximum peaks. The SPL spectra of these LQ controlled flows resemble that previously obtained using a parallel-proportional with time delay feedback control (Yan *et al.* 2006).

Overall, MBF4 produces a marginally improved spectral attenuation compared to that of the MB case. This and the modest performance of the MBF1-3 cases is somewhat surprising, as we would expect the incorporation of open-loop forced flow features to create a richer model capable of delivering better results in closed-loop conditions. The reasons for the lack of significant improvement with respect to the MB model are not clear, but we speculate that they include: (i) the particular technique for control separation that has been employed to render the presence of the control input explicit in the model (Appendix); and (ii) modulation of the control signal introduced by the actuator transfer function. A better resolution of the effect of external forcing may be obtained by resorting to a method of control separation that makes use of 'actuation modes' directly at the level of POD modelling. In addition, the use of a compensator to minimize the frequency modulation of the actuator transfer function could offer significant improvements in controller performance. Both issues are currently being addressed (Caraballo *et al.* 2007; Kim *et al.* 2007).

Having presented the SPL spectra for various reduced-order model based controllers, we now examine in more detail one of the successful cases, MB. Similar

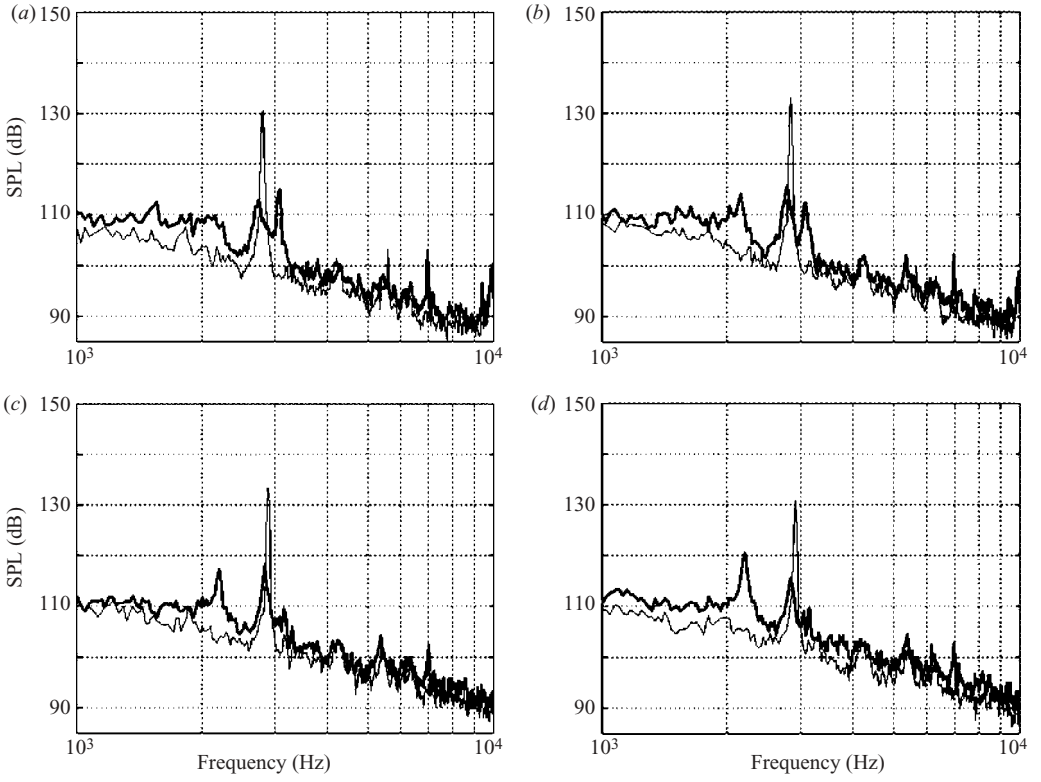


FIGURE 17. SPL spectra from transducer 5. The thin line is the B case and the thick line is control with LQ design based on MB model: (*a*) $M = 0.28$; (*b*) $M = 0.29$; (*c*) $M = 0.31$; (*d*) $M = 0.32$.

to the parallel-proportional control mentioned earlier, the benefits of this scaled LQ controller are retained applying it to slightly off-design conditions around Mach 0.3 (figure 17). In these flows, the feedback controller clearly exhibits a good robustness, whereas F3, which was effective at Mach 0.3, produces a strong forcing peak under the same robustness test. Similar results have also been shown for other open-loop forcing cases (Yan *et al.* 2006). The spectra from the other transducers in the cavity wall are consistent with this observation.

The similarities between the MB control and the parallel-proportional with time-delay control suggest that, although through different processes, similar physical mechanisms are activated at the receptivity region of the cavity shear layer by both these real-time feedback controls. To gain an appreciation of the effects of feedback control on the cavity flow structure, case MB was examined using PIV. As in the open-loop cases (Little *et al.* 2006), the MB controlled flow shows relatively small mean flow variation compared to the resonant baseline case. Figure 18 demonstrates this point using an ensemble average of 1000 velocity profiles at various streamwise locations. The results show that the shear-layer thickness in the two cases is almost the same whereas only small variations in the recirculation region are evident along the downstream half of the cavity. It is surmised that this small variation in recirculation is due to the more steady flow impingement on the cavity trailing edge in the well-controlled flow rather than the periodic impingement seen in the baseline case.

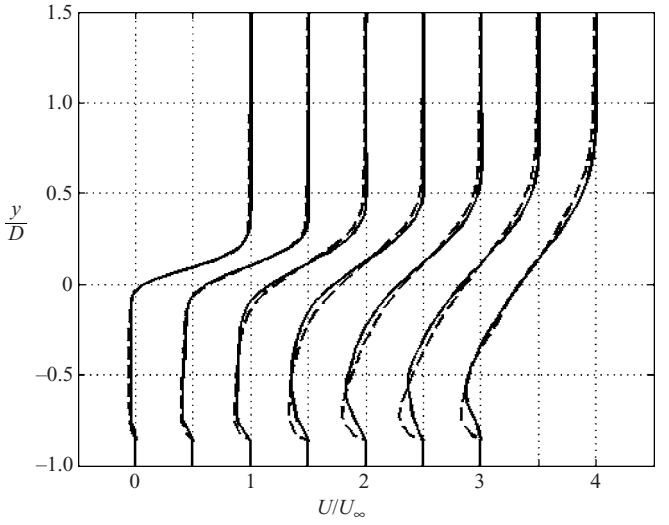


FIGURE 18. Mean streamwise velocity profiles obtained using PIV for —, B and - - -, MB flows. The profiles are taken from left to right at $x/D = 0.5, 0.9, 1.5, 2, 2.5, 3$ and 3.5.

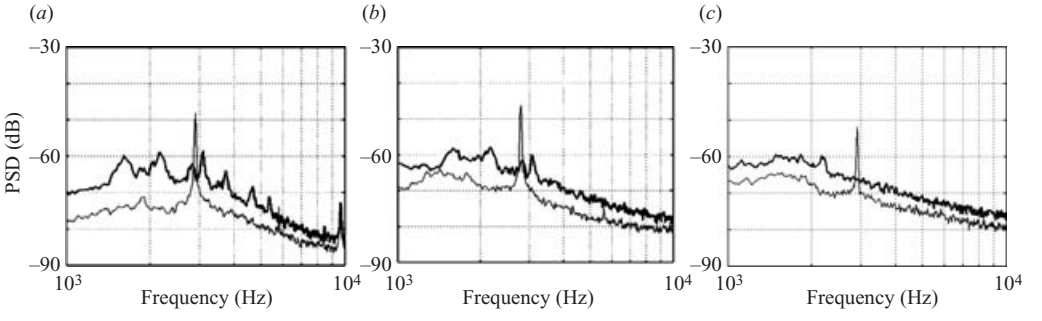


FIGURE 19. Velocity spectra from hot-wire measurements of Mach 0.3 cavity flow at streamwise locations (*a*) $x/D = 1$; (*b*) 2, (*c*) 3. The thin line is the B case and the thick line is case MB.

In the open-loop data presented earlier, a reference signal from the resonating flow or actuator was used to conditionally sample the flow-visualization image or velocity field to obtain phase-averaged data. For a case in which no resonant signal is available (i.e. a well-controlled flow), conditional sampling is not possible experimentally. To circumvent this difficulty and to gain an understanding of the evolution of the cavity shear-layer vortices, we again use a hot-wire survey of the cavity shear layer. The results are presented in figure 19 for three locations along the cavity length, which are striking in comparison to hot-wire data from the baseline flow resonating at the third Rossiter mode. In the upstream region, various frequency components are observed along with much higher broadband velocity fluctuations in comparison to the baseline case. As $x/D$ increases, the frequency content begins to smooth with little to no peaks in the spectrum in the downstream portion of the cavity. This behaviour is also reflected by the SPL spectrum in figure 15 of the controlled flow. Along with the open-loop results presented earlier, these measurements give an indication of one effect of successful control on cavity shear-layer structures. As can be seen from the upstream velocity spectrum (figure 19*a*), there are some frequencies associated with

the large-scale structures in the shear layer; however, owing to the effects of control, these events do not receive sufficient energy from the natural feedback to permit their amplification over the cavity length. Along the downstream half (figure 19*c*), no evident frequency content is visible, implying that, on average, shear-layer vortices break apart before impinging on the downstream corner. This effectively eliminates the possibility of strong acoustic waves at discrete frequencies travelling upstream and thus controls the flow resonance. Other detailed statistical flow properties obtained using PIV and hot wire exhibit some similarities and some differences for the various control cases, which will be further analysed and presented in future publications.

### 6.1. *Concluding remarks*

Comprehensive feedback flow-control work is presented and discussed, which includes (i) acquiring detailed experimental data, (ii) using the experimental data to obtain POD modes to represent the most energetic features in the flow, (iii) projecting tailored Navier–Stokes equations onto the POD modes using the Galerkin projection to obtain reduced-order models of the flow, (iv) using stochastic estimation to correlate the model parameters to surface pressure measurements for real-time model update, (v) designing controllers based on the reduced-order models derived, and as a last step (vi) implementing the controllers to evaluate their performance experimentally. The flow investigated is a subsonic cavity flow. The cavity is shallow with an aspect ratio, $L/D$, of 4 and spans the width of the wind-tunnel test section. The facility can be operated continuously between Mach 0.2 and 0.7, but the majority of the work is carried out around Mach 0.3 with a Reynolds number based on a cavity depth of approximately $10^5$. The output of a compression driver actuator is channelled to the cavity leading edge where it exits at an angle of 30° with respect to the main flow through a thin two-dimensional slot spanning the cavity width. This arrangement provides zero net mass, non-zero net momentum flow for actuation, similar to that of a synthetic jet. Actuation can be achieved in the frequency range of 1–5 kHz with a momentum coefficient in the range of $10^{-4}$ to $10^{-6}$. The baseline cavity flow at Mach 0.3 has a strong single-mode resonance at a frequency of about 2900 Hz corresponding to the third Rossiter mode. Using open-loop sinusoidal forcing, the cavity can be forced to operate at another Rossiter mode or to switch to multi-mode resonance characterized by rapid switching between the modes. These results suggest that one strategy for successful cavity flow control is to excite oscillations at competitive or non-resonant frequencies thereby not supplying sufficient energy or permitting the necessary feedback to allow selective amplification over the extent of the cavity length.

Various laser-based flow diagnostics are used to understand cavity flow physics and to obtain detailed data for the derivation of reduced-order models used in controller design. Particle image velocimetry (PIV) data and the snapshot-based proper orthogonal decomposition (POD) technique are used to extract the most energetic flow features or POD eigenmodes. For each flow case, 1000 PIV snapshots are used to ensure convergence of turbulent kinetic energy. Galerkin projection of the Navier–Stokes equations onto the POD modes is used to derive a set of nonlinear ordinary differential equations that model the time evolution of the modes. Different sets of PIV snapshots of the flow are used to derive reduced-order models for the controller design, including snapshots from the baseline (no actuation) and, the same flow under open-loop forcing at various frequencies. The forced flows include both single-mode and multi-mode regimes. Quadratic stochastic estimation is used

to correlate the model coefficients to dynamic surface pressure measurements, thus enabling a real-time estimate of the state of the models.

Linear-quadratic optimal controllers based on each of these models are designed to control the cavity flow resonance, and are evaluated experimentally. The results obtained with feedback control for some models show a significant attenuation of the resonant tone and a redistribution of the energy into lower-frequency modes with smaller energy levels in both the flow and surface pressure spectra, thereby constituting a significant improvement in comparison with the results obtained with conventional open-loop forcing. Velocity spectra within the shear layer of a feedback-controlled cavity show that some frequencies associated with the large-scale structures exist in the upstream portion of the cavity; however, no resonant frequency content is visible in the downstream half of the cavity. This suggests that, owing to control, large-scale structures do not receive sufficient energy from natural feedback to permit their selective amplification over the cavity length. As with open-loop control, ensemble-averaged streamwise velocity profiles of closed-loop control show small deviations from the baseline, implying that control techniques of this variety affect primarily fluctuating flow properties.

The results presented suggest that feedback control strategies based on reduced-order models represent a compelling approach to subsonic cavity flow control. Notwithstanding the encouraging results reported and discussed in this work, further investigation is required to understand how to incorporate more effectively the presence of actuation in reduced-order POD models. This improvement will allow a more realistic prediction of forced flows while clarifying the interplay between feedforward and feedback control strategies.

This work is supported by the AFRL/VA and AFOSR through the Collaborative Center of Control Science (Contract F33615-01-2-3154). The authors would like to thank Hitay Özbay, James DeBonis, Chris Camphouse, David Williams, Lou Cattefesta, Bernd Noack, Clancy Rowley, Dietmar Rempfer and Gilead Tadmor for help and fruitful discussions.

## Appendix

We describe the procedure used in the derivation of the reduced-order model. The procedure is applied to PIV data (1000 PIV snapshots) taken simultaneously with surface pressure measurements for each flow condition.

### *POD method*

In applying the POD snapshot method to compressible flow it is advantageous to group the independent flow variables and then define an appropriate inner product operator (Freund & Colonius 2002; Rowley 2002). For the case of two-dimensional flow, we define a vector as $\boldsymbol{q}(\boldsymbol{x}, t) = [u(\boldsymbol{x}, t)v(\boldsymbol{x}, t)c(\boldsymbol{x}, t)]$ where $u$, $v$ and $c$ are the local values of the velocity components and of the speed of sound. Following Rowley, Colonius & Morray (2004), the inner product operator is defined in such a way that the final result is dimensionally consistent as

$$\langle \boldsymbol{q}_1, \boldsymbol{q}_2 \rangle_\alpha |_S = \int_S \left( u_1 u_2 + v_1 v_2 + \frac{2\alpha}{\gamma - 1} c_1 c_2 \right) \mathrm{d}\boldsymbol{x} \tag{A 1}$$

where in our study $\alpha = 1$ and $\gamma$ is the ratio of specific heats. The integration is performed over the flow domain $S$.

The POD snapshot approach uses M snapshots of the flow and casts the fluctuations of the flow realizations, $\boldsymbol{q}'(\boldsymbol{x}, t) = [u'v'c']$, in terms of $N < M$ spatial orthonormal modes or POD modes, $\boldsymbol{\varphi}_i(\boldsymbol{x})$, each modulated in time by a modal amplitude $a_i(t)$

$$\boldsymbol{q}'(\boldsymbol{x}, t) \cong \sum_{i=1}^{N} a_i(t)\boldsymbol{\varphi}_i(\boldsymbol{x}). \tag{A 2}$$

Each POD mode is computed as a linear combination of the instantaneous flow fields

$$\boldsymbol{\varphi}_i(\boldsymbol{x}) = \sum_{k=1}^{M} A_{ik}(t)\boldsymbol{q}'(\boldsymbol{x}, t_k) \tag{A 3}$$

with the matrix $\boldsymbol{A}$ obtained by solving the eigenvalue problem

$$\boldsymbol{C}(t, t_k)\boldsymbol{A} = \lambda\boldsymbol{A} \tag{A 4}$$

where $\boldsymbol{C}(t, t_k)$ is the two-point correlation tensor of independent snapshots integrated over the spatial domain of interest, defined as

$$\boldsymbol{C}(t, t_k) = \frac{1}{M}\langle \boldsymbol{q}(\boldsymbol{x}, t), \boldsymbol{q}(\boldsymbol{x}, t_k)\rangle|_S. \tag{A 5}$$

The $i$th modal amplitude of a known flow field, $\boldsymbol{q}'(x, t)$, can be obtained from

$$a_i(t) = \int_s \boldsymbol{q}'(\boldsymbol{x}, t)\boldsymbol{\varphi}_i(\boldsymbol{x})\,\mathrm{d}\boldsymbol{x}. \tag{A 6}$$

*Galerkin projection and low-dimensional model*

The Galerkin projection method is used to obtain a reduced-order model of flow dynamics, which consists of a system of ordinary nonlinear differential equations for the modal amplitude $\boldsymbol{a}(t) = [a_1(t)\, a_2(t) \ldots a_N(t)]$. The method relies on the projection of the governing equations of the flow, the compressible Navier–Stokes equations, onto the orthogonal basis of POD modes. In our study we adopted the two-dimensional form of the Navier–Stokes equations based on the work of Rowley (2002)

$$\left.\begin{aligned} \frac{\mathrm{D}c}{\mathrm{D}t} + \frac{\gamma - 1}{2}c\nabla\cdot\boldsymbol{u} = 0, \\ \frac{\mathrm{D}u}{\mathrm{D}t} + \frac{2}{\gamma - 1}c\nabla c = \frac{\mu}{\rho}\nabla^2\boldsymbol{u}, \end{aligned}\right\} \tag{A 7}$$

where $\boldsymbol{u} = (u, v)$.

The Galerkin projection procedure involves the following general steps. The flow variables are first expressed in terms of their mean component and of the POD expansion of their fluctuating components from (A 2)

$$\boldsymbol{q}(\boldsymbol{x}, t) = \boldsymbol{q}_m(\boldsymbol{x}) + \sum_{i=1}^{N} a_i(t)\boldsymbol{\varphi}_i(\boldsymbol{x}) \tag{A 8}$$

where $\boldsymbol{q}_m$ denotes the mean flow. Replacing the terms from (A 8) in the governing equations (A 7) leads to an expression of the form

$$\sum_{i=1}^{N} \dot{a}_i(t)\boldsymbol{\varphi}_i(\boldsymbol{x}) = f\left\{\boldsymbol{q}(\boldsymbol{x}, t), \frac{\partial}{\partial x}q(\boldsymbol{x}, t), \ldots\right\} \equiv \boldsymbol{f}(\boldsymbol{x}, t), \tag{A 9}$$

where the left-hand side stems from the time derivatives in (A 7) and the right-hand side groups all the other terms of (A 7). In the Galerkin projection, the inner products according to (A 1) of both sides of (A 9) are taken with the POD modes. Because of the orthonormality of the modes, the only terms surviving on the left-hand side correspond to the modes projecting onto themselves

$$\dot{a}_i(t) = \langle \boldsymbol{\varphi}_i(\boldsymbol{x}),\, f(\boldsymbol{x},t)\rangle|_S \quad (i = 1, 2, \ldots, N). \tag{A 10}$$

We modified the above process in order to obtain a set of equation where the control effect appears explicitly. The procedure, presented in more detail in Efe & Özbay (2003) and Samimy *et al.* (2003), separates the control input of the system by dividing the entire flow domain into two distinct sub-domains. One smaller region, $S_2$, comprises the physical region where the synthetic jet excitation is dominant whereas a second larger region, $S_1$, contains the rest of the flow field. The total flow domain can then be expressed as $S := S_1 \cup S_2$.

It is important to notice that $\langle \boldsymbol{\varphi}_i(\boldsymbol{x}),\, \boldsymbol{f}(\boldsymbol{x},t)\rangle|_S = \langle \boldsymbol{\varphi}_i(\boldsymbol{x}),\, \boldsymbol{f}(\boldsymbol{x},t)\rangle|_{S_1} + \langle \boldsymbol{\varphi}_i(\boldsymbol{x}),\, \boldsymbol{f}(\boldsymbol{x},t)\rangle|_{S_2}$ holds true by the definition of the inner product. Therefore, (A 10) can be more explicitly written as

$$\dot{a}_i(t) = \langle \boldsymbol{\varphi}_i(\boldsymbol{x}),\, \boldsymbol{f}(\boldsymbol{x},t)\rangle|_{S_1} + \langle \boldsymbol{\varphi}_i(\boldsymbol{x}),\, \boldsymbol{f}(\boldsymbol{x},t)\rangle|_{S_2} \quad (i = 1, 2, \ldots, N). \tag{A 11}$$

Since the boundary excitation $\Gamma(t)$ accounts for the flow characteristics in the $S_2$ subdomain, we can write

$$\boldsymbol{q}_m(\boldsymbol{x})|_{S_2} + \sum_{i=1}^{N} a_i(t)\, \boldsymbol{\varphi}_i(\boldsymbol{x})|_{S_2} = \Gamma(t) \tag{A 12}$$

and in (A 11), the terms corresponding to the left-hand side of (A 12) can be replaced with the excitation $\Gamma(t)$. With this modification and depending on the form of the vector function $\boldsymbol{f}$, the procedure described will yield a non-autonomous set of ODEs capturing the dynamics in the following form

$$\dot{a}_i(t) = F^i + \sum_{j=1}^{N} G^{ij} a_j(t) + \sum_{j=1}^{N}\sum_{k=1}^{N} H^{ijk} a_j(t) a_k(t) + B^i \Gamma(t) + \sum_{j=1}^{N} \bar{B}^{ij} \Gamma(t) a_j(t). \tag{A 13}$$

The Galerkin model in the form of (A 13) can be also compactly expressed in the vector notation

$$\dot{\boldsymbol{a}} = \boldsymbol{A}(\boldsymbol{a}) + \boldsymbol{B}(\boldsymbol{a})\Gamma \tag{A 14}$$

where,

$$\boldsymbol{A}(a) = \boldsymbol{F} + \boldsymbol{G}\boldsymbol{a} + \boldsymbol{a}^T \boldsymbol{H}\boldsymbol{a}, \tag{A 15}$$

$$\boldsymbol{B}(\boldsymbol{a}) = \boldsymbol{B} + \bar{\boldsymbol{B}}\boldsymbol{a}. \tag{A 16}$$

Equation (A 14) represents the reduced-order model sought for the design of a feedback controller.

*Stochastic estimation*

For the quadratic SE, the expression used to estimate $\hat{a}_i(t_r)$ at any time $t$ is

$$\hat{a}_i(t) = C^{ij} p'_j(t) + D^{ijk} p'_j(t) p'_k(t) \quad (i = 1, \ldots, N, \quad j, k = 1, \ldots, \mathscr{L}), \tag{A 17}$$

where $\boldsymbol{C}$ and $\boldsymbol{D}$ are the matrices of the estimation coefficients obtained by minimizing the average mean square error $e_i$ between the values of $a_i$ $(t_r)$ obtained with (A 6) at

the times $t_r$ of the PIV snapshot, and those $\hat{a}_i(t_r)$ estimated from the pressure data recorded simultaneously with the snapshots. That is,

$$e_i = \langle [\hat{a}_i(t_r) - a_i(t_r)]^2 \rangle \quad (r = 1, \ldots, M), \tag{A 18}$$

where the operator $\langle\ \rangle$ (not to be confused with the inner product previously defined) represents the time average of its arguments. Once the estimation matrices $\boldsymbol{C}$ and $\boldsymbol{D}$ are obtained, they can be replaced in (A 17) to estimate the modal amplitude from the surface pressure measurements.

## REFERENCES


Adrian, R. J. 1979 *On the Role of Conditional Averages in Turbulent Theory. Turbulence in Liquids.* Science Press, Princeton.

Adrian, R. J. & Moin, P. 1988 Stochastic estimation of organized turbulent structure: homogeneous shear Flow. *J. Fluid Mech.* **190**, 531–559.

Alvarez, J. & Kerschen, E. 2005 Influence of wind tunnel walls on the cavity acoustic resonances. *AIAA Paper* 2005-2804.

Alvarez, J., Kerschen, E. & Tumin, A. 2004 A theoretical model for cavity acoustic resonances in subsonic flows. *AIAA Paper* 2004-2845.

Ausseur, J. M., Pinier, J. T., Glauser, M. N., Higuchi, H. & Carlson, H. 2006 Experimental development of a reducer-order model for flow separation control. *AIAA Paper* 2006-1251.

Berkooz, G., Holmes, P. & Lumley, J. L. 1993 The proper orthogonal decomposition in the analysis of turbulent flows. *Annu. Rev. Fluid Mech.* **25**, 539–575.

Cabell, R. H., Kegerise, M. A., Cox, D. E. & Gibbs, G. P. 2002 Experimental feedback control of flow induced cavity Tones. *AIAA Paper* 2002-2497.

Caraballo, E., Malone, J., Samimy, M. & Debonis, J. 2004 A study of subsonic cavity flows – low dimensional modeling. *AIAA Paper* 2004-2124.

Caraballo, E., Yuan, X., Little, J., Debiasi, M., Yan, P. Serrani, A., Myatt, J. & Samimy, M. 2005 Feedback control of cavity flow using experimental based reduced order model. *AIAA Paper* 2005-5269.

Caraballo, E., Yuan, X., Little, J., Debiasi, M., Serrani, A., Myatt, J. & Samimy, M. 2006 Further development of feedback control of cavity flow using experimental based reduced order model. *AIAA Paper* 2006-1405.

Caraballo, E., Little, J., Debiasi, M., Serrani, A. & Samimy, M. 2007 Reduced-order model for feedback control of cavity flow – the effects of control input separation. *AIAA Paper* 2007-1125.

Cattafesta III, L. N., Garg, S., Choudhari, M. & Li, F. 1997 Active control of flow-induced cavity resonance. *AIAA Paper* 1997-1804.

Cattafesta, L., Garg, S., Kegerise, M. & Jones, G. 1998 Experiments on compressible flow-induced cavity resonance. *AIAA Paper* 1998-2912.

Cattafesta, L., Shukla, D., Garg, S. & Ross, J. 1999 Development of an adaptive weapons-bay suppression system. *AIAA Paper* 1999-1901.

Cattafesta III, L. N., Williams, D. R., Rowley, C. W. & Alvi, F. S. 2003 Review of active control of flow-induced cavity resonance. *AIAA Paper* 2003-3567.

Citriniti, J. & George, W. 2000 Reconstruction of the global velocity field in the axisymmetric mixing layer utilizing the proper orthogonal decomposition. *J. Fluid Mech.* **418**, 137–166.

Cole, D. R. & Glauser, M. N. 1998 Application of stochastic estimation in the axisymmetric sudden expansion. *Phys. Fluids* **10** (11), 2941–2949.

Debiasi, M. & Samimy, M. 2004 Logic-based active control of subsonic cavity flow resonance. *AIAA J.* **42**, 1901–1909.

Debiasi, M., Little, J., Malone, J., Samimy, M., Yan, P. & Özbay, H. 2004 An experimental study of subsonic cavity flow – physical understanding and control. *AIAA Paper* 2004-2123.

Delville, J., Cordier, L. & Bonnet, J. P. 1998 Large-scale-structure identification and control in turbulent shear flows. In *Flow Control: Fundamentals and Practice* (ed. M. Gad-el-Hak, A. Pollard & J. Bonnet), pp. 199–273. Springer.

Efe, M. Ö. & Özbay, H. 2003 Proper orthogonal decomposition for reduced order modeling: 2D heat flow. *IEEE Intl Conf. on Control Applications (CCA 2003), Istanbul, Turkey*, pp. 1273–1278.

Efe, M., Debiasi, M., Yan, P., Özbay, H. & Samimy, M. 2005 Control of subsonic cavity flows by neural networks-analytical models and experimental validation. *AIAA Paper* 2005-0294.

Freund, J. & Colonius, T. 2002 POD analysis of sound generation by a turbulent jet. *AIAA Paper* 2002–72.

Gad-el-Hak, M. 2000 *Flow Control – Passive, Active, and Reactive Flow Management*. Cambridge University Press.

Gerhard, J., Pastoor, M., King, R., Noack, B., Dillmann, A., Morzynski, M. & Tadmor, G. 2003 Model-based control of vortex shedding using low-dimensional Galerkin models. *AIAA Paper* 2003-4262.

Glauser, M., Eaton, E., Taylor, J., Cole, D., Ukeiley, L., Citriniti, J., George, W & Stokes, S. 1999 Low-dimensional descriptions of turbulent flows: experiment and modeling. *AIAA Paper* 1999-3699.

Glauser, M. N., Higuchi, H., Ausseur, J. & Pinier, J. 2004 Feedback control of separated flows. *AIAA Paper* 2004-2521.

Grove, J., Leugers, J. & Akroyd, G. 2003 USAF/RAAF F-111 flight test with active separation control. *AIAA Paper* 2003-0009.

Hammond, J. K. & White, P. R. 1996 The analysis of non-stationary signals using time-frequency methods. *J. Sound Vib.* **190**, 419–447.

Heller, H. H. & Bliss, D. B. 1975 The physical mechanisms of flow-induced pressure fluctuations in cavities and concepts for their suppression. *AIAA Paper* 1975-491.

Holmes, P., Lumley, J. L. & Berkooz, G. 1996 *Turbulence, Coherent Structures, Dynamical System, and Symmetry*. Cambridge University Press.

Hussain, A. & Zaman, K. 1985 An Experimental study of organized motions in the turbulent plane mixing layer. *J. Fluid Mech.* **159**, 85–104.

Kegerise, M., Cattafesta, L. & Ha, C. 2002 Adaptive identification and control of flow-induced cavity oscillations. *AIAA Paper* 2002-3158.

Kerschen, E. & Tumin, A. 2003 A theoretical model of cavity acoustic resonances based on edge scattering processes. *AIAA Paper* 2003-0175.

Kim, K., Debiasi, M., Serrani, A., & Samimy, M. 2007 System identification and feedback control of a synthetic jet-like compression driver actuators. *AIAA Paper* 2007-0880.

Little, J., Debiasi, M. & Samimy, M. 2006 Flow structure in controlled and baseline subsonic cavity flows. *AIAA Paper* 2006-0480.

Lumley, J. 1967 *The structure of inhomogeneous turbulent flows. Atmospheric turbulence and Wave Propagation* pp. 166–176. Nauca, Moscow.

Mcgrath, S. & Shaw, L. 1996 Active control of shallow cavity acoustic resonance. *AIAA Paper* 1996-1949.

Murray, N. & Ukeiley, L. 2002 Estimating the shear layer velocity field above an open cavity from surface pressure measurements. *AIAA Paper* 2002-2866.

Naguib, A., Wark, C. & Juckenhoefel, O. 2001 Stochastic estimation and flow sources associated with surface pressure events in a turbulent boundary layer. *Phys. Fluids* **13** (9), 2611–2616.

Noack, B., Tadmor, G. & Morzynski, M. 2004 Low-dimensional models for feedback flow control. Part I: Empirical Galerkin models. *AIAA Paper* 2004-2408.

Picard, C. & Delville, J. 2000 Pressure velocity coupling in a subsonic round jet. *Intl J. Heat Fluid Flow* **21**, 359–364.

Qian, S & Chen, D.1996 *Joint Time–Frequency Analysis*. Prentice-Hall.

Rockwell, D. & Naudascher, E. 1978 Review – self-sustaining oscillations of flow past cavities. *Trans. ASME* I: *J. Fluids Engng* **100**, 152–165.

Rossiter, J. E. 1964 Wind tunnel experiments on the flow over rectangular cavities at subsonic and transonic speeds. RAE Tech. Rep. 64037, and Aeronautical Research Council Reports and Memoranda No. 3438.

Rowley, C. W. 2002 Modeling, simulation and control of cavity flow oscillations. PhD thesis, California Institute of Technology.

Rowley, C., Colonius, T. & Morray, R. 2004 Model reduction for compressible flow using POD and Galerkin projection. *Physica* D **189**, 115–129.

Rowley, C. & Williams, D. 2003 Control of forced and self-sustained oscillations in the flow past a cavity. *AIAA Paper* 2003-0008.

Rowley, C. & Williams, D. 2006 Dynamics and control of high-Reynolds-number flow over open cavities. *Annu. Rev. Fluid Mech.* **38**, 251–276.

Rowley, C. W., Williams, D. R., Colonius, T., Murray, R. M., Macmartin, D. G. & Fabris, D. 2002 Model-based control of cavity oscillations. Part II: System identification and analysis. *AIAA Paper* 2002-0972.

Samimy, M., Debiasi, M., Caraballo, E., Özbay, H., Efe, M. O., Yuan, X., Debonis, J. & Myatt, J. H. 2003 Closed-loop active flow control: a collaborative approach. *AIAA Paper* 2003-0058.

Samimy, M., Debiasi, M., Caraballo, E., Malone, J., Little, J., ÖZbay, H., Efe, M. Ö., Yan, P., Yuan, X., Debonis, J., Myatt, J. H. & Camphouse, R. C. 2004 Exploring strategies for closed-loop cavity flow control. *AIAA Paper* 2004-0576.

Sarno, R. & Franke, M. 1994 Suppression of flow-induced pressure oscillations in cavities. *J. Aircraft* **31**, 90–96.

Shaw, L. 1998 Active control for cavity acoustics. *AIAA Paper* 1998-2347.

Shaw, L. & Northcraft, S. 1999 Closed loop active control for cavity resonance. *AIAA Paper* 1999-1902.

Siegel, S., Cohen, K., Seidel, J. & Mclaughlin, T. 2003 Feedback control of a circular cylinder wake in experiments and simulations. *AIAA Paper* 2003-3569.

Siegel, S., Cohen, K., Seidel, J. & Mclaughlin, T. 2005 Two dimensional simulations of a feedback controlled D-cylinder wake. *AIAA Paper* 2005-5019.

Sirovich, L. 1987 Turbulence and the dynamics of coherent structures. *Q. Appl. Maths* **45**, 561–590.

Stanek, M. J., G., Kibens, V., Ross, J. A., Odedra, J. & Peto, J. W. 2003 High frequency acoustic suppression – the mystery of the rod-in-crossflow revealed. *AIAA Paper* 2003-0007.

Tadmor, G., Noack, B., Morzynski, M. & Siegel, S. 2004 Low-dimensional models for feedback flow control. Part II: Control design and dynamical estimation. *AIAA Paper* 2004-2409.

Ukeiley, L. & Murray, N. 2005 Velocity and surface pressure measurements in an open cavity. *Exps. Fluids* **38**, 656–671.

Ukeiley, L. S., Ponton, M. K., Seiner, J. M. & Jansen, B. 2002 Suppression of pressure loads in cavity flows. *AIAA Paper* 2002-0661.

Williams, D., Fabris, D. & Morrow, J. 2000 Experiments on controlling multiple acoustic modes in cavities. *AIAA Paper* 2000-1903.

Williams, D. R., Rowley, C., Colonius, T., Murray, R., Macmartin, D., Fabris, D. & Albertson, J. 2002 Model-based control of cavity oscillations. Part I: Experiments. *AIAA Paper* 2002-0971.

Yan, P., Debiasi, D. Yuan, X., Little, J., Özbay, H. & Samimy, M. 2006 Closed-loop linear control of cavity flow. *AIAA J.* **43**, 929–938.

Yuan, X. , Caraballo, E., Yan, P., Özbay, H., Serrani, A., Debonis, J., Myatt, J. H. & Samimy, M. 2005 Reduced-order model-based feedback controller design for subsonic cavity flows. *AIAA Paper* 2005-0293.

Ziada, S., Ng, H. & Blake, C. 2003 Flow excited resonance of a confined shallow cavity in low Mach number flow and its control. *J. Fluids Struct.* **18**, 79–82.